











# NAVAL POSTGRADUATE SCHOOL

## Monterey , California



## THESIS

M18963

THERMAL IMAGING  
WITH  
AGA THERMOVISION 780

by

Tim R. McKaig

v v v

December 1987

Thesis Advisor:

A.W. Cooper

Approved for public release; distribution is unlimited.

T239081



## REPORT DOCUMENTATION PAGE

1a REPORT SECURITY CLASSIFICATION UNCLASSIFIED			1b RESTRICTIVE MARKINGS	
2a SECURITY CLASSIFICATION AUTHORITY			3 DISTRIBUTION/AVAILABILITY OF REPORT Approved for public release; distribution is unlimited	
2b DECLASSIFICATION/DOWNGRADING SCHEDULE			5 MONITORING ORGANIZATION REPORT NUMBER(S)	
4 PERFORMING ORGANIZATION REPORT NUMBER(S)			7a NAME OF MONITORING ORGANIZATION Naval Postgraduate School	
6a NAME OF PERFORMING ORGANIZATION Naval Postgraduate School		6b OFFICE SYMBOL (If applicable) 61	7b ADDRESS (City, State, and ZIP Code) Monterey, California 93943-5000	
6c ADDRESS (City, State, and ZIP Code) Monterey, California 93943-5000			9 PROCUREMENT INSTRUMENT IDENTIFICATION NUMBER	
8a NAME OF FUNDING SPONSORING ORGANIZATION		8b OFFICE SYMBOL (If applicable)	10 SOURCE OF FUNDING NUMBERS	
8c ADDRESS (City, State, and ZIP Code)			PROGRAM ELEMENT NO	PROJECT NO
			TASK NO	WORK UNIT ACCESSION NO
11 TITLE (Include Security Classification) THERMAL IMAGING WITH AGA THERMOVISION 780				
12 PERSONAL AUTHOR(S) McKaig, Tim R.				
13a TYPE OF REPORT Master's Thesis		13b TIME COVERED FROM TO	14 DATE OF REPORT (Year, Month, Day) 1987 December	15 PAGE COUNT 88
16 SUPPLEMENTARY NOTATION This work was funded by NEPRF under program 62435N, Project RM35G80 "BATTLE GROUP ENVIRONMENTAL SUPPORT IN ATMOSPHERIC PREDICTIONS."				
17 COSATI CODES			18 SUBJECT TERMS (Continue on reverse if necessary and identify by block number)	
FIELD	GROUP	SUB-GROUP	Thermal Imaging, Thermal Radiation, AGA Thermovision 780	
			Minimum Resolvable Temperature Difference	
19 ABSTRACT (Continue on reverse if necessary and identify by block number) Thermal images of a ship target were recorded with an AGA Thermovision 780 thermal imaging system on 6-13 May 1987. These images were used to produce temperature distributions of the ship. The temperatures predicted with the AGA computer-processing algorithm were compared to actual temperatures measured with thermistors at eight locations on the ship's superstructure. An empirical modification based on the identity of the ambient and local atmospheric conditions was developed for the atmospheric compensation algorithm. The predicted temperatures were found to agree with the actual temperatures within 1.5 °C in 77 percent of the measurements. The Contrast Transfer Function (CTF), Modulation Transfer Function (MTF), and Minimum Resolvable Temperature Difference (MRTD) were determined for the Thermovision using flat black painted aluminum bar targets. The resultant curves showed the expected form with some experimental scatter at higher spatial frequencies.				
20 DISTRIBUTION/AVAILABILITY OF ABSTRACT <input type="checkbox"/> UNCLASSIFIED/UNLIMITED <input type="checkbox"/> SAME AS RPT <input type="checkbox"/> DTIC USERS			21 ABSTRACT SECURITY CLASSIFICATION unclassified	
22a NAME OF RESPONSIBLE INDIVIDUAL A.W. Cooper			22b TELEPHONE (Include Area Code) (408) 646-2452	22c OFFICE SYMBOL 61Cr

Approved for public release; distribution unlimited

Thermal Imaging  
with  
AGA Thermovision 780

by

Tim R. McKaig  
Captain, United States Army  
B.S., United States Military Academy, 1978

Submitted in partial fulfillment of the  
requirements for the degree

MASTER OF SCIENCE IN PHYSICS

from the

NAVAL POSTGRADUATE SCHOOL  
December 1987



## ABSTRACT

Thermal images of a ship target were recorded with an AGA Thermovision 780 thermal imaging system on 6-13 May 1987. These images were used to produce temperature distributions of the ship. The temperatures predicted with the AGA computer-processing algorithm were compared to actual temperatures measured with thermistors at eight locations on the ship's superstructure. An empirical modification based on the identity of the ambient and local atmospheric conditions was developed for the atmospheric compensation algorithm. The predicted temperatures were found to agree with the actual temperatures within 1.5 °C in 77 % of the measurements. The Contrast Transfer Function (CTF), Modulation Transfer Function (MTF), and Minimum Resolvable Temperature Difference (MRTD) were determined for the Thermovision using flat black painted aluminum bar targets. The resultant curves showed the expected form with some experimental scatter at higher spatial frequencies.

## TABLE OF CONTENTS

I.	INTRODUCTION.....	7
II.	PERTINENT THEORY.....	10
	A. THERMAL RADIATION LAWS.....	10
	B. NATURAL RADIATION SOURCES.....	12
	C. ATMOSPHERIC PROPAGATION OF THERMAL RADIATION.....	15
	D. PERFORMANCE MEASURES OF THERMAL IMAGING SYSTEMS.....	18
III.	DESCRIPTION OF AGA THERMOVISION 780.....	25
	A. GENERAL.....	25
	B. DUAL SCANNER.....	25
	C. BLACK AND WHITE MONITOR CHASSIS.....	26
	D. IF 800 MICROCOMPUTER.....	27
	E. TEMPERATURE MEASUREMENT TECHNIQUE.....	27
IV.	ACQUIRED DATA.....	31
	A. RECORDING OF SHIP IMAGES.....	31
	B. EVALUATION OF SHIP IMAGES.....	32
	C. THERMISTOR DATA.....	36
	D. CTF, MTF, AND MRTD CURVES.....	37
V.	ANALYSIS OF DATA.....	42
	A. GENERAL.....	42
	B. REVIEW OF THERMOVISION'S THERMAL MEASUREMENT PROCESS.....	42
	C. REVISED TEMPERATURE DISTRIBUTIONS.....	44

D.	PRECISION ESTIMATES FOR THERMAL MEASUREMENTS.....	46
E.	REVIEW OF THERMOVISION VS. THERMISTER TEMPERATURE DIFFERENCES.....	47
F.	MTF AND MRTD CURVES.....	48
VI.	CONCLUSIONS AND RECOMMENDATIONS.....	51
A.	SUMMARY.....	51
B.	CONCLUSIONS.....	52
C.	RECOMMENDATIONS.....	53
	APPENDIX A: FIGURES.....	55
	APPENDIX B: TABLES.....	77
	LIST OF REFERENCES.....	86
	INITIAL DISTRIBUTION LIST.....	87

## ACKNOWLEDGEMENTS

This work was funded by the Naval Environmental Prediction Research Facility, Monterey, CA under Program Element 62435N, Project # RM35G80 "BATTLE GROUP ENVIRONMENTAL SUPPORT IN ATMOSPHERIC PREDICTIONS".

The author would like to acknowledge the extensive technical assistance provided by Jerry Lentz and Bob Sanders, without whose contributions this thesis would not have been possible. The advice provided by Professor E. C. Crittenden, particularly during the construction of the Thermovision's Contrast Transfer Function curve, was certainly appreciated. Finally, the author's most sincere gratitude is extended to Professor A. W. Cooper for his thoughtful direction during all phases of this work. Professor Cooper has made the study of Infrared science a thoroughly enjoyable and beneficial experience.

## I. INTRODUCTION

Thermal imaging is the process of collecting thermal radiation emitted by an object and producing a visible image of that object. Although the concept is simple, implementation of a thermal imaging device quickly becomes a complicated venture. First, the designer is confronted with a relatively broad portion of the electromagnetic spectrum, the infrared region; therefore, he must consider target radiation characteristics in the design process. Second, the target must be recognized against a background of several natural radiation sources. These sources include celestial emissions, the sun, the sky, and terrestrial materials. Finally, the atmosphere attenuates target radiation by scattering and absorption mechanisms. Most current thermal imagers utilize quantum detectors to collect infrared radiation from a scene and convert this information to analog electrical signals which are processed and displayed on a video monitor. The ability of a detector to recognize a target depends on image contrast, i.e. the difference between target emittance and the background emittance. Because thermal radiation is a function of an emitter's temperature, the effective temperature difference between target and background provides a good measure of image contrast provided the emissivity differences are not great.



The apparent temperature perceived by an imaging device can vary considerably from the actual temperature. This irregularity is primarily due to background and atmospheric effects. If a designer is able to predict the impact of these effects accurately, then the imaging device will be better able to match perceived target temperatures with actual target temperatures.

This thesis explored the differences between the apparent temperatures sensed by a thermal imaging system and the actual temperatures of a target. The imaging system used was an AGA Thermovision 780, manufactured by the AGEMA Corporation. The target was the R/V Point Sur, an oceanographic ship operated by the National Science Foundation for the Naval Postgraduate School and Moss Landing Marine Laboratory. The background was Monterey Bay in two vicinities: the Moss Landing Marine Laboratory and the Hopkins Marine Station. Data were taken during May 1987. Also, the Thermovision's Modulation Transfer Function (MTF) and Minimum Resolvable Temperature Difference (MRTD) curves were determined using square aluminum plates painted with bars of flat black paint. The use of aluminum permitted adequate heat transfer across a plate, so that the temperature was constant at all portions of the plate. The emissivities of the paint and aluminum were substantially different which caused a radiation contrast to exist between the bars of paint and bars of exposed aluminum.

Chapter II details the theory behind thermal radiation, atmospheric propagation of such radiation, and thermal imaging system performance measures. Chapter III describes the technical characteristics and operational capabilities of the Thermovision 780, as well as the temperature measurement techniques of the system. Chapter IV contains the results of the experiment, while the analysis of these results is presented in Chapter V. The conclusions and recommendations of this thesis follow in Chapter VI.

## II. PERTINENT THEORY

### A. THERMAL RADIATION LAWS

Thermal radiation is comprised of photons that are emitted by molecules undergoing vibrational and rotational transitions. These molecules may be the original sources of the photons or they may be reradiating photons emitted from other sources. In macroscopic terms, objects can be self-emitting thermal radiation sources or reflectors of such radiation. Most objects in our environment exhibit both mechanisms. [Ref. 1:p. 18]

Several physical laws have been developed that describe the nature of thermal radiation. Foremost is Planck's radiation law which gives the spectral distribution of radiant emittance,  $W_\lambda$ . This law is:

$$W_\lambda[\lambda, T] = (2\pi hc/\lambda^5) \frac{1}{[\exp(ch/\lambda kT) - 1]} \quad (\text{Watt/m}^2 - \mu\text{m}) \quad (2-1)$$

where  $k$  is Boltzmann's constant,  $c$  is the speed of light in a vacuum, and  $h$  is Planck's constant. Figure 2.1 [Ref. 1: p. 23] depicts spectral emittance for three object temperatures. When this expression is differentiated and set equal to zero, Wien's displacement law is obtained. This is:

$$\lambda_m T = 2897.8 \quad (\mu\text{m-K}) \quad (2-2)$$

where  $\lambda_m$  is the most abundant wavelength of radiation for a

particular temperature. This thesis deals with the 8-14 micrometer band of radiation which corresponds to a temperature range of 207.0-362.2 K, temperatures that clearly exist in our environment. This is a good indication of the background problem that confronts thermal imaging systems.

Integrating the expression for Planck's law across the entire spectrum of wavelengths yields the Stefan-Boltzmann law, given by:

$$W(T) = (2\pi^5 k^4) / (15c^2 h^3) T^4 = \sigma T^4 \quad \{\text{Watt/m}^2\} \quad (2-3)$$

where  $W(T)$  is radiant emittance and  $\sigma$  is the Stefan-Boltzmann constant. Radiation sources are commonly described in terms of radiance,  $L(T)$ , which is radiant emittance through a unit solid angle. Many sources effectively radiate into a hemisphere as perfectly rough planes. Radiance for such a Lambertian surface is:

$$L(T) = W(T) / \pi \quad \{\text{watt/m}^2\text{-steradian}\} \quad (2-4)$$

Most objects in our environment do not emit as ideal blackbodies, but emit only a fraction of the blackbody radiant power. This fraction is known as the "emissivity" and can range in value from zero (a perfect reflector) to one (a black body). Thus, the Stefan-Boltzmann law becomes:

$$W(T) = \epsilon \sigma T^4 \quad (2-5)$$

where  $\epsilon$  is the emissivity of an object. For an object in

thermal equilibrium with its surroundings, the object's absorbed power must equal the emitted power. This leads to Kirchoff's law which is:

$$\varepsilon(\lambda) = \alpha(\lambda) \quad (2-6)$$

where  $\alpha(\lambda)$  is the object's spectral absorptivity.

Thermal radiation impinging on an object can undergo one of three mechanisms. First, the radiation can be absorbed and subsequently reradiated as described by Kirchoff's law. Second, the radiation can be reflected off the object. Third, the radiation can be transmitted through the object. Hence, the boundary conditions at an object's surface are described by the total power law:

$$\alpha(\lambda) + \rho(\lambda) + T(\lambda) = 1 \quad (2-7)$$

where  $\rho(\lambda)$  is the spectral reflectivity and  $T(\lambda)$  is the spectral transmissivity.

## B. NATURAL RADIATION SOURCES

Celestial background radiation includes infrared emission from solid material within our galaxy, as well as from extragalactic sources. Irradiance levels from celestial sources have been found to be around  $10^{-16}$  W/cm<sup>2</sup>- $\mu$ m for the 3 to 26 micrometer region [Ref. 2:p. 3-28]. Such levels are several orders of magnitude lower than those of other sources; therefore, celestial sources will not be considered in this thesis.



The sun can be treated approximately as a blackbody at 5900 K, when the earth's atmospheric effects are ignored. Figure 2.2 [Ref. 2:p. 3-34] depicts the spectral irradiance of the sun outside and within the earth's atmosphere. At 5900 K the most abundant wavelengths radiating from the sun are in the visible region; however, a small percentage of the sun's spectral emittance is in the infrared region i.e., 0.0986 percent in the 8-14 micrometer band, which equates to 133.5 W/m<sup>2</sup> [Ref. 2:p.3-36]. Contributions of the sun to background radiation must be considered during daylight hours and particularly in background scenes that approach the sun's direction.

The sky contributes to the background radiation through the scattering of solar radiation and emission from atmospheric constituents [Ref. 2:p. 3-71]. Figure 2.3 [Ref. 2:p. 3-71] depicts these contributions as well as solar radiation and radiation from a cloud. The presence of clouds affects both the scattering of near-infrared solar radiation and the sky's thermal radiation. Forward scattering in clouds is prevalent in the near-infrared region; however, multiple scattering dominates the forward scattering effects in a heavily overcast sky. The spectral emittance due to the sky emissions approaches that of a black body at atmospheric temperature in bands of high atmospheric absorption.

Optically thick clouds are also well represented by a black body curve based on a cloud's average temperature;

however, the "wings" of this curve correspond to regions of high atmospheric absorption. Accordingly, the black body curve in these "wings" is based on the atmospheric temperature rather than the cloud's temperature. Figure 2.4 [Ref. 2:p. 3-73] illustrates this effect of a cumulus cloud radiating as a blackbody at one temperature and the sky radiating as a black body at different temperature.

While the radiation of numerous terrestrial materials could be examined, only that of marine backgrounds will be considered in this thesis. The marine background is affected by four factors: the optical properties of water; the surface geometry and wave slope distribution; surface temperature distribution; and bottom material properties [Ref. 2:p. 3-105].

Sea water has very low transmittance and reflectance values in the infrared region. The exception is that high reflectances do exist at large angles of incidence. When the sea surface is roughened by wind, the reflectance is significantly reduced at angles of incidence near the horizon. Figure 2.5 [Ref. 2:p. 3-106] depicts reflectivity and emissivity of smooth water versus angle of incidence.

As with any thermal emitter, the sea surface temperature determines the radiant emittance of the sea. The temperature gradient is quite pronounced in the upper 1.0 mm of the surface due to the cooling effects of evaporation. Figure 2.6 [Ref. 2:p. 3-109] depicts this gradient. The gradient is

much less at lower depths but can be influenced by the convective activity of the water. Surface temperatures can be altered by surface contamination which restricts the flow of heat from lower depths; thus the apparent surface temperature will be lower than the bulk water temperature [Ref. 2:p. 3-109].

Because sea water has such low transmittance values for the infrared region, the properties of bottom materials have negligible effects on the background radiation.

### C. ATMOSPHERIC PROPAGATION OF THERMAL RADIATION

The transmittance of the earth's atmosphere is less than one, since the atmosphere does not behave as a perfect dielectric. This transmittance is given by the Lambert-Beer law:

$$T_A(\lambda) = \exp[-\mu(\lambda)R] \quad (2-8)$$

where  $T_A(\lambda)$  is the extinction coefficient and  $R$  is the distance of propagation. The average transmittance for a particular bandwidth  $\lambda_1$  to  $\lambda_2$  is:

$$T_A = \frac{1}{\lambda_2 - \lambda_1} \int_{\lambda_1}^{\lambda_2} \exp[-\mu(\lambda)R] d\lambda \quad (2-9)$$

Extinction of thermal radiation is caused by absorption and scattering processes. Thus, the extinction coefficient is given by the expression:

$$\mu(\lambda) = k(\lambda) + \alpha(\lambda) \quad (2-10)$$

where  $k(\lambda)$  is the absorption coefficient and  $\alpha(\lambda)$  is the scattering coefficient. Both coefficients have components due to air molecules, as well as aerosol particles. Therefore:

$$k(\lambda) = k_m(\lambda) + k_a(\lambda) \quad (2-11)$$

and

$$\alpha(\lambda) = \alpha_m(\lambda) + \alpha_a(\lambda) \quad (2-12)$$

where the subscripts  $m$  and  $a$  denote molecule and aerosol respectively. The values of these coefficients have been empirically determined and depend on the density and composition of both the molecules and aerosols.

Molecular absorption is due primarily to water, carbon dioxide, ozone, nitrous oxide, carbon monoxide, and methane [Ref. 2:pp. 5-101 - 5-105]. These absorbers limit thermal radiation in the atmosphere to two windows: the 3.5-5.0 and 8-14 micrometer bands.

Aerosols have been categorized in four standard types. Maritime aerosols are made up primarily of salt particles which act as condensation centers for water. The concentration of these particles is largely dependent on wind speed, while the size distribution is influenced by relative humidity. Continental aerosols consist of silicon, iron, sulphates, and organic material. One third of these aerosols can act as condensation centers. Urban aerosols are composed

of combustion and industrial products. Stratospheric aerosols contain sulphate with an occasional addition of volcanic dust. [Ref. 3: p. 17-14]

Scattering by molecules in the 8-14 micrometer band is relatively insignificant. Wavelengths in this region are much larger than particle size, so that Rayleigh scattering would be valid. However, the  $\lambda^{-4}$  dependence of Rayleigh scattering reduces the effect of molecular scattering. Mie scattering theory pertains to particles of all sizes; therefore, it is valid for aerosols. Because Mie scattering is somewhat independent of wavelength in the large particle limit, aerosol scattering is quite significant in the 8-14 micrometer band. Mie scattering is most effective around  $r/\lambda \sim 1$ , while particle size distributions extend out to tens of micrometers.

Due to the complex nature of atmospheric propagation of thermal radiation, several computer models have been developed to predict atmospheric transmittance. LOWTRAN 6 is the model which will be used in this thesis. LOWTRAN is a FORTRAN based code that calculates atmospheric transmittance and radiance for a specified range of wavelengths along a designated path length. Seven atmospheric models are available including the U.S. Standard Atmosphere and a model based on user specified meteorological data.



#### D. PERFORMANCE MEASURES OF THERMAL IMAGING SYSTEMS

A fundamental parameter restricting performance of any imaging system is contrast. In the case of thermal imagers, radiation contrast is used to assess how well a target can be seen against its background. The expression for radiation contrast,  $C$ , is:

$$C = (W_T - W_B) / (W_T + W_B) \quad (2-13)$$

where  $W_T$  is the target radiant emittance and  $W_B$  is background radiant emittance. Figure 2.7 [Ref. 1:p. 29] shows radiation contrast curves for four background temperatures.

The radiation contrast of bar targets can be used to construct a Contrast Transfer Function (CTF). As a bar target represents a square wave input to an imaging system, the CTF describes the system's square wave amplitude response at the spatial frequency of that target [Ref. 4:p. 114]. The CTF of a system is determined by plotting the radiation contrast for a range of spatial frequencies. The resultant function has an initial value of 1.0 (100 percent contrast) at zero spatial frequency and drops to a final value of 0.0 (no contrast) at the system's cutoff frequency, i.e. the maximum spatial frequency above which a system can no longer resolve a test target.

A more useful measure of a system's resolution capability is the Modulation Transfer Function (MTF). "The MTF is the sine-wave spatial frequency response" [Ref. 4:p. 114]. The

MTF can be determined from the CTF using the following relationship [Ref. 4:p.117]:

$$M(f) \sim (\pi/4)[C(f) + C(3f)/3 - C(5f)/5 + C(7f)/7] \quad (2-14)$$

where  $M(f)$  is the value of the MTF at a single spatial frequency,  $f$ .  $C(f)$  is the value of the CTF at that frequency. Figure 2.8 [Ref. 1:p. 19] contains an MTF curve for an example imaging system.

While the MTF is a valuable measure, it describes only a small part of an imaging system's ability to perform intended tasks. Ideally, a performance measure must be based on fundamental system parameters and "must relate to the performance of the system as it is intended." The most widely used performance measure for infrared detection systems is Noise Equivalent Temperature Difference (NETD). NETD is a measure of a system's ability to detect small signals in noise. NETD is the target-to-background temperature difference that corresponds to a system's peak signal to rms noise ratio equal to one. [Ref. 1:p. 166]

NETD is derived from an expression for spectral irradiant power received by the detector. Such an expression would be:

$$P_{\lambda}(\lambda, T) = [W_{\lambda}(\lambda, T)/\pi] \Omega A_T T_O \quad \{\text{Watt}/\mu\text{m}\} \quad (2-15)$$

where  $W_{\lambda}(\lambda, T)$  is the target's spectral emittance,  $\Omega$  is the solid angle subtended by the system's optical aperture,  $A_T$  is the target area from which radiation is received by the

system's optical aperature, and  $T_0$  is the system optical transmission. Since the solid angle is  $A_0/R^2$  and the target area is  $\alpha\beta R^2$ , equation 2-15 can be written as:

$$P_\lambda = (W_\lambda/\pi) A_0\alpha\beta T_0 \quad (2-16)$$

where  $A_0$  is the area of the optical aperature and  $\alpha$  and  $\beta$  are the system's horizontal and vertical subtense angles.

The target's differential change in irradiant power with respect to temperature is of primary interest. By differentiating equation 2-16 with respect to temperature, such an expression is found:

$$\partial P_\lambda/\partial T = [(\alpha\beta A_0 T_0)/\pi] \partial W_\lambda/\partial T \quad (2-17)$$

The system's differential change in signal voltage is found by multiplying equation 2-17 by the system's responsivity,  $R(\lambda)$ , a parameter that gives the ratio of signal voltage output to incident power:

$$\partial V_S/\partial T = R(\lambda) [(\alpha\beta A_0 T_0)/\pi] \partial W_\lambda/\partial T \quad (2-18)$$

Responsivity is given by:

$$R(\lambda) = [V_n D^*(\lambda)] / (ab B_n)^{1/2} \quad (2-19)$$

where  $V_n$  is the detector rms noise voltage produced by  $B_n$ , the noise bandwidth of a test reference filter,  $a$  and  $b$  are detector dimensions, and  $D^*(\lambda)$  is the system's specific

detectivity. Inserting equation 2-19 into 2-18 yields:

$$\partial V_S / \partial T = D^*(\lambda) (\alpha \beta A_O T_O) / [\pi (ab B_N)^{1/2}] \partial W_\lambda / \partial T \quad (2-20)$$

Assuming small target-to-background temperatures, the temperature differential of target emittance can be approximated by the derivative of Planck's law at the background temperature  $T_B$ :

$$\partial W_\lambda / \partial T \sim (c_2 / \lambda T_B^2) W_\lambda(T_B) \quad (2-21)$$

where  $c_2 = 1.4388 \times 10^4 \mu\text{m-K}$ . Specific detectivity can also be written as:

$$\begin{aligned} D^*(\lambda) &= \lambda D^*(\lambda_p) / \lambda_p & \text{for } \lambda \leq \lambda_p \\ &= 0 & \text{for } \lambda \geq \lambda_p \end{aligned} \quad (2-22)$$

where  $\lambda_p$  is the wavelength corresponding to the peak value of system detectivity. Inserting equations 2-21 and 2-22 into equation 2-20 and integrating across the effective waveband  $\lambda_1$  to  $\lambda_p$  yields:

$$\partial V_S / \partial T = \frac{\alpha \beta A_O T_O V_N}{\pi (ab B_N)^{1/2}} \frac{D^*(\lambda_p)}{\lambda_p} \frac{c_2}{T_B^2} \int_{\lambda_1}^{\lambda_p} W_\lambda(T_B) d\lambda \quad (2-23)$$

Assuming a small signal approximation and rearranging equation 2-23 produces an expression for the signal-to-noise ratio:

$$\text{SNR} = \Delta V_S / V_N = \Delta T \frac{\alpha \beta A_O T_O}{\pi (ab B_N)^{1/2}} \frac{D^*(\lambda_p) c_2}{\lambda_p T_B^2} \int_{\lambda_1}^{\lambda_p} W_\lambda(T_B) d\lambda \quad (2-24)$$

Based on the definition of NETD, the SNR is set equal to one and  $\Delta T$  becomes NETD. Thus, NETD in final form for a scanning imager is:

$$\text{NETD} = \frac{\pi(abB_n)^{1/2}}{\alpha\beta T_o} \frac{\lambda_p T_B^2}{D^*(\lambda_p)c_2} \left[ \int_{\lambda_1}^{\lambda_p} w_\lambda(T_B) d\lambda \right]^{-1} \quad \{K\} \quad (2-25)$$

Although NETD is a satisfactory measure of a system's target detection capability, it is of limited utility for thermal imagers because this measure does not account for image quality. A more appropriate performance measure for these devices is Minimum Resolvable Temperature Difference (MRTD) which incorporates the system MTF and provides a measure of how well an imaging system can resolve a target. MRTD is defined as the blackbody target-to-background temperature difference in a standard test pattern at which an observer viewing the system display can resolve a target [Ref 1:pp. 190-192].

An analytical expression for MRTD is based on a system's signal-to-noise ratio in the image of one bar. This ratio is:

$$\text{SNR}_i = 4/\pi M(f) [\Delta T/(\text{NETD})] (\rho^{1/2})^{-1} \quad (2-26)$$

where  $M(f)$  is the system modulation of the image (i.e. MTF), the  $\Delta T/\text{NETD}$  factor is the electronic SNR measured at a NETD reference filter with a target-to-background temperature difference  $\Delta T$ , and  $\rho^{1/2}$  is the ratio of actual system bandwidth to reference bandwidth.



As the observer views the target, this perceived SNR is modified by four factors. First, the eye operates on a mean signal rather than peak signal; therefore, the SNR is reduced by a factor of  $2/\pi$ . Second, the SNR is improved by a temporal integration factor of  $(T_e F)^{1/2}$  where  $T_e$  is the effective eye integration time and  $F$  is the system frame rate. Third, the SNR is improved by the eye's spatial integration of the bar height which is seven times greater than the bar width. This factor is  $(7/2 f\beta)^{1/2}$ . Finally, the bandwidth ratio is improved by the eye's matched filter action. [Ref. 1:p. 186]

A good approximate value of the perceived SNR has been found to be 4.5 for a 90% probability of detection [Ref. 1:p. 188]. Using this value and the observer's perception factors, equation 2-26 is rearranged so that:

$$\text{MRTD}(f) = \Delta T = \frac{3 \text{ NETD}}{M(f)} \rho_m^{1/2} \frac{(f\beta)^{1/2}}{(T_e F)^{1/2}} \quad (2-27)$$

where  $\rho_m^{1/2}$  is the improved bandwidth ratio due to the eye's matched filter action. Because the displayed noise in many systems is white [Ref. 1:p. 189],  $\rho_m^{1/2}$  can be given by the simple expression:

$$\rho_m^{1/2} = (4\alpha f/\pi)^{1/2} \quad (2-28)$$

Inserting equation 2-28 into 2-27, the final expression for MRTD becomes:

$$\text{MRTD}(f) = \frac{6 \text{ NETD } f(\alpha\beta)^{1/2}}{M(f) (\pi T_e F)^{1/2}} \quad \{K\} \quad (2-29)$$

Figure 2.8 contains an MRTD curve for an example imaging system.

The NETD listed for the AGA Thermovision 780 is 0.12 °C at 22 °C [Ref. 5]. The MRTD is not provided by the manufacturer but was determined during the experimental portion of this thesis. These results are found in Chapter IV. The MRTD deduced is then applied to the discussion of the measured temperature distributions in Chapter V.

### III. DESCRIPTION OF AGA THERMOVISION 780

#### A. GENERAL

The AGA Thermovision 780 thermal imaging system incorporates a dual scanner which senses thermal radiation in two spectral bands and produces electronic video signals. These signals are amplified and used to display images on a black and white monitor. The scanner and monitor are shown in Figure 3.1 [Ref. 6]. The system is augmented with a microcomputer that displays digitized pictures of the system's video on a color monitor and records these pictures onto a floppy disk. The computer uses a software program that color codes each picture according to the scene's temperature distribution. A schematic of the total Thermovision system is displayed in Figure 3.2 [Ref. 7].

#### B. DUAL SCANNER

The dual scanner is actually comprised of two scanning systems. The shortwave system, 3 to 5.6 micrometer, has a single Indium Antimonide photovoltaic detector and silicon lens. The longwave system, 8 to 14 micrometer, has a single Mercury Cadmium Telluride detector and germanium lens. Each system has a  $7^{\circ} \times 7^{\circ}$  field of view with a standard lens. A  $3.5^{\circ} \times 3.5^{\circ}$  lens is also available for the long wave system. Each system uses vertical and horizontal scanning prisms to produce a 4 to 1 interlaced raster scan. Each of the four

fields has 100 scanning lines, although only 70 lines are used to produce images. The interlaced frame in this configuration consists of 280 scanning lines. The detectors are cooled to 77 K with Dewar flasks containing liquid nitrogen.

### C. BLACK AND WHITE MONITOR CHASSIS

The dual scanner is connected to two black and white monitors, so that scenes in the two spectral bands can be viewed simultaneously. The monitor chassis contains controls for adjusting the brightness and contrast of the display. The chassis also contains controls for adjusting the thermal level and thermal range of the system. These two adjustments are measured in Thermal Units which are arbitrary units of measure proportional to the intensity of the system's received thermal radiation. The thermal level control adjusts the DC level of the AC video signal, while the thermal range control limits the dynamic range of this signal.

These controls can be used in conjunction with a calibration plot to assess manually the temperature distribution of a scene. The relationship between thermal level and thermal range settings versus temperature is shown in the calibration curve enclosed as Figure 3.3 [Ref. 6]. A change in thermal level corresponds to a nonlinear change in scene temperatures the Thermovision can sense. An adjustment of the thermal range determines the measurable temperature

range which is approximately centered about the "median" temperature established by the thermal level setting.

#### D. IF 800 MICROCOMPUTER

A BMC IF 200 microcomputer processes the infrared data for the AGA Thermovision 780 and provides an automated means of assessing temperature distributions. On command, the computer's DISCO 3.0 program (AGEMA Corporation proprietary software) creates an eight color picture based on thermal values provided by the system and parameters inserted by the user. The color scheme depicts the temperature distribution of a scene with each color representing a particular temperature range. The program provides temperature data to the user in several formats. The feature utilized in this thesis is the ability to assess the temperature associated with each pixel in the display screen comprised of an array of 128 X 128 pixels.

The computer in this temperature evaluation mode displays a crosshair which is moved about the screen by means of four cursor control keys. The user positions the crosshair over a particular pixel and the computer displays the pixel's temperature in the lower right corner of the screen.

#### E. TEMPERATURE MEASUREMENT TECHNIQUE

The thermal measurement technique utilized by the Thermovision 780 is based on the relation:

$$P_i = T_a \epsilon_o P_o + T_a (1 - \epsilon_o) P_s + (1 - T_a) P_a \quad \{\text{Watt}\} \quad (3-1)$$



where  $P_i$  is the total radiant power received by the system,  $P_o$  is the radiant power from the object as a blackbody,  $P_s$  is the radiant power from the object's surroundings as a blackbody,  $P_a$  is the radiant power from the atmosphere as a blackbody,  $T_a$  is the atmospheric transmittance, and  $\epsilon_o$  is the object's emissivity. The emissivity of the surroundings and atmosphere are assumed to be one.

The first term on the right hand side of equation 3-1 is the received radiant power emitted by the object. The second term is the received radiant power emitted by the object's surroundings and reflected by the object. The third term is received radiant power emitted by the atmosphere.

Because the system's thermal value measure is proportional to received radiant power, equation 3-1 can be written as:

$$I_i = T_a \epsilon_o I_o + T_a (1 - \epsilon_o) I_s + (1 - T_a) I_a \text{ \{Thermal Units\} } \quad (3-2)$$

where the  $I$  terms represent the thermal values of corresponding radiation sources. The received thermal value consists of two terms such that:

$$I_i = L + i \quad (3-3)$$

where  $L$  is the thermal level setting on the monitor chassis and  $i$  is a fractional portion of the thermal range.

Substituting equation 3-3 into 3-2 and manipulating terms yields the following expression for the object's thermal

value:

$$I_o = (L+i)/T_a \epsilon_o - (1/\epsilon_o - 1)I_s - 1/\epsilon_o(1/T_a - 1)I_a \quad (3-4)$$

The thermal values in the above expression are dependent on corresponding temperatures. The thermal value-temperature relationship is calibrated under laboratory conditions using the equation:

$$I = A / [C \exp(B/T) - 1] \quad (3-5)$$

where A, B, and C are calibration constants. The resultant calibration curves are similar to that shown in Figure 3.3. Equation 3-5 is used by the system to convert atmospheric and ambient temperatures to corresponding thermal values and to convert I to an object temperature.

The atmospheric transmission factor is approximated by the system using:

$$T_a = \exp[-\alpha(\sqrt{d}-1)] \quad (3-6)$$

where  $\alpha$  is an atmospheric attenuation constant and d is the distance to object. The value of  $\alpha$  specified by the manufacturer is 0.008 for the long waveband. A more accurate transmission factor can be computed using the LOWTRAN propagation code which is based on a form of Beer's law as given in equation 2-8:

$$T_a(\lambda) = \exp[-\mu(\lambda)R] \quad (3-7)$$

where  $\mu(\lambda)$  is the atmospheric extinction factor that represents scattering and absorption effects as discussed in Chapter II. Values based on this equation will be used in this thesis.

#### IV. ACQUIRED DATA

##### A. RECORDING OF SHIP IMAGES

The AGA Thermovision 780 was used to record thermal images in the 8-14 micrometer band of the R/V Point Sur at the Moss Landing location on 6 May and 13 May 1987 and at the Hopkins Marine Station on 9 and 11 May 1987. The map in Figure 4.1 depicts these locations on Monterey Bay and the approximate direction in which the Thermovision was aimed. Images were recorded with the ship presenting various aspects; however, only images of the ship at a 90° aspect were evaluated in this thesis. The Point Sur was instrumented with eight thermistors to measure the temperatures of various parts of the ship. These temperatures would be used as a basis of comparison for temperatures sensed by the Thermovision. Weather balloons were launched prior to each recording period. The radiosonde data recorded by the balloons were used as input to the LOWTRAN 6 program to determine atmospheric transmittance values. These data are contained in Table 1.

Images were recorded with the Thermovision's thermal range setting on two, five, and 10 Thermal Units; however, only those images recorded at the setting of five were used to evaluate temperature distributions of the ship. A thermal range of two Thermal Units did not correspond to a large enough temperature range in order to measure the entire ship.

A thermal range of 10 Thermal Units produced images with poorer temperature resolution than those images recorded at a setting of five Thermal Units.

## B. EVALUATION OF SHIP IMAGES

Before the recorded images could be evaluated for temperature distributions, the Thermovision had to be initialized with the following values: the ambient air temperature around the ship; the atmospheric temperature; the emissivity of the ship; the range of the ship; and the atmospheric transmittance. The values of ambient temperature and the atmospheric temperature were assumed to be equal and were based on the air temperatures reported by ship personnel. These temperatures are contained in Table 2. The emissivity of the ship was assumed to be 0.95 as previously determined and reported [Ref. 9]. The range of the ship from the Thermovision's location was determined by measuring the length of the ship's image on the Thermovision's display screen and inserting this value into the following trigonometric relation:

$$R = (S_0 / \tan \theta) (S_i / w)^{-1} = (w S_0 / \tan \theta) 1 / S_i \quad \{m\} \quad (4-1)$$

where R is the ship's range, w is the display screen width (13cm),  $S_0$  is the ship length (41.2m),  $\theta$  is the system field of view ( $7^\circ$ ), and  $S_i$  is the image length in cm. Inserting values for the constants, equation 4-1 becomes:

$$R = (4354 / S_i) \pm 20 \quad \{m\} \quad (4-2)$$



where the uncertainty in range was based on the differential method of error estimation.

As mentioned previously, the transmittance values were calculated with the LOWTRAN 6 code. The atmospheric model was based on radiosonde data collected by the weather balloons. The Navy maritime aerosol model was used which incorporated three aerosol components: a continental component; a "stationary" component produced by winds and whitecaps; and a "fresh" component formed by current conditions [Ref. 3:p. 17-35].

An air mass character of 2 was selected for the Moss Landing location, while an air mass character of 4 was selected for the Hopkins Marine Station. The air mass character was a subjective rating of continental influence on maritime aerosols on a scale of one to 10. A rating of one would represent an open ocean, while ten would indicate strong continental influence. As can be seen in the map enclosed as Figure 4.1, the Moss Landing location was quite exposed to the open ocean, while the Hopkins Marine Station was somewhat protected by the Monterey Peninsula.

A horizontal path was specified with an altitude of 5 m. The range was based on the predicted range for a given image. Calculated transmittance values are contained in Table 2.

The Thermovision's image evaluation program also had to be calibrated to a reference heat source prior to evaluation of the Point Sur images. The calibration was conducted on

13 October 1987 using a black body heat source adjusted to temperatures ranging from 6.0 °C to 30.0 °C. The black body consisted of a hollow aluminum cylinder covered with fiberglass insulation. The cylinder was 28 cm long and 7.5 cm in diameter. A 2 cm entrance hole was located in the front of the cylinder. The rear surface was canted, so that incident light normal to the entrance hole would not be reflected out of the cylinder. A thermocouple was attached to the rear of the cylinder for the purpose of measuring the black body temperature. The interior of the cylinder was painted flat black.

The calibration was conducted in a laboratory with a room temperature of 18.8 °C. In order to cool the black body to below room temperature, liquid nitrogen was poured into the cylinder until the black body temperature was 2 °C. As the black body warmed to room temperature, the Thermovision was used to record images of the black body at 1 °C increments starting at 6 °C. In order to warm the black body above room temperature, the cylinder was wrapped with a nichrome wire. The wire ends were connected to a variac, so that the current generated would heat the cylinder. Again the Thermovision was used to record images of the black body in 1 °C increments up to 30 °C.

Once the black body images were recorded for each temperature, the Thermovision's image evaluation program was used to predict the black body temperatures. The results of

the calibration process are contained in Table 3. These results were used to produce the calibration curve shown in Figure 4.2. This curve was subsequently used to convert temperatures computed with the Thermovision method to values that more closely approximated actual temperatures.

The temperature distributions of the Point Sur were developed using a 6 X 15 element array. This array configuration was based on the Point Sur's approximate height to length ratio of 1/5. The vertical and horizontal dimensions were multiplied by factors of six and three respectively in order to facilitate the presentation of distributions on 8 1/2" X 11" notebook paper. In this configuration one distribution element approximately represented a 2.75 m X 1.35 m portion of the ship's surface area at 90° aspect. Images used to produce these distributions were recorded during the following times:

DATE	TIME	SIDE OF SHIP
6 May	1857	Starboard
6 May	1901	Portside
9 May	1128	Portside
9 May	1140-1141	Starboard
11 May	0944-0948	Starboard
11 May	1004-1008	Portside
13 May	1520-1521	Starboard
13 May	1526	Portside

The temperature distributions for these periods are found in Figures 4.3 through 4.6. An anomaly was found during the initial review of these distributions. The inconsistency pertained to Figure 4.3 which portrayed the Point Sur's temperature distribution for 6 May. Some temperatures of the ship's upper superstructure in this figure were lower than the ambient air temperature. Physically, this situation would not be possible. The Point Sur had no known heat sinks in this portion of the ship; therefore, ship temperatures could equal or exceed the ambient air temperature, but would not be less than the air temperature. The conclusion drawn from Figure 4.3 was that the Thermovision might have been underestimating actual temperatures. This problem had to be resolved before any detailed analysis of the Point Sur's temperature distributions could be made.

#### C. THERMISTOR DATA

The thermistor resistance values were recorded by microcomputer throughout the time the Point Sur was at sea. The locations of the eight thermistors are indicated in Figure 4.7. After the cruise these values were converted to temperature values and averaged for the time periods corresponding to those periods for which the Thermovision was recording images. Actually, the thermistor averaging time was extended two minutes prior to and two minutes after the the image recording period. The averaged thermistor temperatures with standard deviations are found in Table 4.

These averaged temperatures were then compared with the temperatures computed by the Thermovision for areas of the ship where the thermistors had been located. The temperature differences between the thermistor-measured temperatures and the Thermovision-computed temperatures are listed in Table 5. These differences were quite significant on 6 May and 13 May. The Thermovision underestimated the thermistor-measured temperatures by an average of 4.5 °C on 6 May and 4.7 °C on 13 May. This situation reinforced the tentative conclusion that the Thermovision was underestimating actual temperatures.

#### C. CTF, MTF, AND MRTD CURVES

Because a Minimum Resolvable Temperature Difference (MRTD) curve was not provided by the manufacturer, one was produced for the purposes of this thesis. As discussed in Chapter II, the MRTD curve provides a good measure of a system's resolution capability. Since the MRTD curve is based on a system Modulation Transfer Function (MTF), the Thermovision's MTF had to be determined. A system Contrast Transfer Function (CTF) was more readily attainable; therefore, the system CTF was determined and the MTF computed from this curve.

A Contrast Transfer Function (CTF) for the Thermovision was determined on 19 October 1987. The CTF was based on values of radiation contrast for targets of various spatial frequencies as described in Chapter II. The targets consisted



of 1/8 inch thick square aluminum plates with four bars of flat black paint applied. The emissivity of the paint was estimated at 0.95 and the emissivity of the aluminum was estimated at 0.30 [Ref. 10]. Thus, a target appeared to the Thermovision as a standard seven bar target as depicted in Figure 4.8 [Ref. 1:p. 76]. Bar widths ranged in size from 5 mm to 120 mm. The targets were placed at distances ranging from 1 m to 4 m. The following relation was used to generate 28 various spatial frequencies:

$$f = d / 2w \quad \text{(cycles/radian)} \quad (4-3)$$

where  $f$  is spatial frequency,  $d$  is distance between target and Thermovision optics, and  $w$  is target bar width.

With the laboratory room temperature at 18.8 °C the targets were heated to 25 °C. A thermocouple was bolted to the center of each target to measure target temperature. While the Thermovision was imaging a bar target, an oscilloscope was used to measure the radiation contrast between bars. The oscilloscope was connected to a video output port of the analogue-to-digital convertor and set to display target signal voltage. The intensity profile in Figure 4.8 depicts how a bar target would appear on the oscilloscope display. The heights of the signal peak and minimum were measured and equation 2-8 used to calculate radiation contrast.

$$C = (W_T - W_B) / (W_T + W_B) \quad (2-8)$$

In this case  $W_T$  was proportional to the emittance of the black bars of paint and  $W_B$  was proportional to the emittance of the aluminum bars. (Note: The vertical distance on the oscilloscope display was proportional to signal voltage and thus target emittance.) Since the target temperature and background temperature were equal, the radiation contrast could be written as:

$$C = (\epsilon_T \sigma T_T^4 - \epsilon_B \sigma T_B^4) / (\epsilon_T \sigma T_T^4 + \epsilon_B \sigma T_T^4) \\ = (\epsilon_T - \epsilon_B) / (\epsilon_T + \epsilon_B) \quad (4-4)$$

The values of radiation contrast for various spatial frequencies are listed in Table 6. These values were normalized relative to 4 cycles/radian, the frequency at which the bar target consisted of one black bar and one aluminum bar. This target filled the system's entire field of view, hence this was the minimum spatial frequency that could be viewed by the Thermovision. The normalized radiation contrast values were then used to calculate the MTF values for each spatial frequency based on equation 2-14:

$$M(f) \sim (\pi/4)[C(f) + C(3f)/3 - C(5f)/5 + C(7f)/7] \quad (2-14)$$

CTF and MTF values are found in Table 7. Finally, the MRTD was calculated for each spatial frequency using equation 2-29:

$$MRTD(f) = \frac{6 \text{ NETD } f(\alpha\beta)^{1/2}}{M(f) (\pi T_e F)^{1/2}} \quad (2-29)$$

The NETD for the Thermovision was listed by the manufacturer as 0.12 °C at a background temperature of 22 °C. However, the MRTD calculated in this thesis was based on a background temperature of 18.8 °C; therefore, a correction factor was needed. This factor was readily computed using the expression for NETD found in equation 2-25:

$$\text{NETD} = \frac{\pi(abB_n)^{1/2}}{\alpha\beta A_o T_o} \frac{\lambda_p T_B^2}{D^* (\lambda_p) c_2} \left[ \int_{\lambda_1}^{\lambda_p} w_\lambda(T_B) d\lambda \right]^{-1} \quad (2-25)$$

The factor dependent on background temperature was:

$$\text{CF}(T_B) = T_B^2 \left[ \int_{\lambda_1}^{\lambda_p} w_\lambda(T_B) d\lambda \right]^{-1} \quad (4-5)$$

The denominator of this factor was integrated from  $\lambda_1 = 8 \mu\text{m}$  to  $\lambda_p = 10 \mu\text{m}$  with a hand-held calculator using Simpson's rule. The corrected NETD was:

$$\begin{aligned} \text{NETD}(18.8 \text{ } ^\circ\text{C}) &= \frac{\text{CF}(18.8 \text{ } ^\circ\text{C})}{\text{CF}(22 \text{ } ^\circ\text{C})} \text{NETD}(22 \text{ } ^\circ\text{C}) = 0.985 (0.12 \text{ } ^\circ\text{C}) \\ &\sim 0.12 \text{ } ^\circ\text{C} \end{aligned}$$

Thus, the NETD was essentially unchanged.

The following Thermovision parameters were inserted into equation 2-29:

$$\text{NETD} = 0.12 \text{ } ^\circ\text{C}$$

$$\alpha = \beta = 1.1 \text{ mrad}$$

$$T_e = 0.2 \text{ sec}$$

$$F = 6.25 \text{ frames/sec}$$

Thus, the expression for MRTD became:

$$\text{MRTD} = 4.00 \times 10^{-4} \quad f/M(f) \quad \{^{\circ}\text{C}\} \quad (4-6)$$

MTF and MRTD values are found in Table 8. A plot of the system CTF, MTF and MRTD values are found in Figures 4.9, 4.10, and 4.11.

## V. ANALYSIS OF DATA

### A. GENERAL

As discussed in Chapter IV, the data presented in Figure 4.3 and Table 5 showed that the Thermovision-sensed temperatures were substantially lower than the actual temperatures measured by the thermistors on the four days of data recording. The average Thermovision-thermistor temperature differences were  $-4.5^{\circ}\text{C}$ ,  $-1.9^{\circ}\text{C}$ ,  $-1.1^{\circ}\text{C}$ , and  $-4.7^{\circ}\text{C}$  respectively. An explanation was needed as to why the Thermovision was underestimating target temperatures.

### B. REVIEW OF THERMOVISION'S THERMAL MEASUREMENT PROCESS

As detailed in Chapter III, the Thermovision computes object temperatures based on two equations:

$$I_i = T_a \epsilon_o I_o + T_a (1 - \epsilon_o) I_s + (1 - T_a) I_a \quad (3-2)$$

and

$$I = A [C \exp(B/T) - 1]^{-1} \quad (3-5)$$

The first term on the right hand side of equation 3-2 represents radiation emitted by the target. The middle term represents radiation from the target's ambient atmosphere that reflects off the target and propagates to the Thermovision. The third term represents atmospheric radiation received by the Thermovision.



In this thesis  $I_s$  was assumed to equal  $I_a$ , i.e. the atmosphere was treated as a continuum extending from the target's surroundings to the Thermovision. Thus equation 3-2 becomes:

$$I_i = T_a \epsilon_o I_o + T_a (1 - \epsilon_o) I_a + (1 - T_a) I_a \quad (5-1)$$

Based on this assumption, equations 3-2 and 5-1 had a shortcoming. First, the middle term on the right hand side of these equations had an implicit value of atmospheric emittance equal to unity, i.e. the ambient atmosphere was treated as a black body. The third term on the right hand side of these equations had  $1 - T_a$  as the emittance of the atmosphere existing between the Thermovision and target. Since the ambient atmosphere and the atmosphere between the Thermovision and target were to be treated as one body, both portions would have to have the same emittance. This emittance would be  $1 - T_a$ . The original assumption that the ambient atmosphere emitted as a black body is invalid. Thus, equation 5-1 becomes:

$$I_i = T_a \epsilon_o I_o + T_a (1 - T_a) (1 - \epsilon_o) I_a + (1 - T_a) I_a \quad (5-2)$$

This equation was used to recalculate temperatures in the temperature distributions; however, the discrepancy was still not resolved. The approach at this point was to fit empirically the thermistor temperature data to a modified version of equation 5-2. This required setting the first  $T_a$

term of the middle term on the right hand side of equation 5-2 to one. Based on this change and a combination of like terms, equation 5-2 becomes:

$$I_i = T_a \epsilon_o I_o + (1 - T_a)(2 - \epsilon_o) I_a \quad (5-3)$$

Theoretically, this modification could not be justified but it did result in good agreement between Thermovision-computed temperatures and thermister measured temperatures. The implication of equation 5-3 is that the atmosphere exhibited no attenuation of ambient radiation reflected from the target.

#### C. REVISED TEMPERATURE DISTRIBUTIONS

Utilizing equations 5-3 and 3-5, temperature distributions of the Point Sur were recalculated with a Hewlett-Packard Model 97 programmable calculator. The revised distributions are enclosed as Figures 5.1 through 5.4.

A number of observations about these distributions could be made. The warmest part of the ship was usually the smoke stack area which had temperatures clearly exceeding 20 °C in most cases. The one exception was the starboard side on 6 May. Element B7 was the warmest part in this case (19.8 °C).

Excluding the smoke stack, the warmest part of the ship varied from day to day. These areas are indicated below:

DATE	LOCATION (element)	SIDE	TEMPERATURE
6 May	B7	Starboard	19.8 °C
9 May	A11	Port	20.4 °C
11 May	B8,B9	Starboard	20.8 °C
13 May	C2	Starboard	20.7 °C

The higher temperature associated with row A (just above the water line) were most likely due to additional thermal radiation from the ship reflecting off the sea surface. The higher temperatures associated with row B corresponded to an enclosed portion of the ship. Apparently, heat was transferred from these enclosed spaces to the outer surface of the ship. The higher temperature at C2 was possibly due to solar glint.

The coolest part of the ship also varied on a daily basis. These areas are noted below:

DATE	LOCATION (element)	SIDE	TEMPERATURE
6 May	C13	Starboard	15.2 °C
9 May	A2	Starboard	13.8 °C
11 May	A15	Port	14.3 °C
13 May	A2	Port	14.8 °C

Generally, these cooler portions were at extreme points on the ship's superstructure. Exposure to the open air or sea surface at these points probably resulted in greater heat dissipation than at other locations of the ship.

A final note on the distributions is that the temperature difference between adjacent distribution elements rarely

exceeded the estimated deviation in temperature due to experimental error (1.5 °C) except around the smoke stack; however, the range of temperatures within the entire distribution, disregarding the smoke stack, clearly exceeded this error estimate in all cases. This range was 4.6 °C, 6.6 °C, 6.5 °C, and 5.9 °C respectively for each of the four days.

#### D. PRECISION ESTIMATES FOR THERMAL MEASUREMENTS

The estimate of experimental error was based on the differential method using equations 5-1 and 3-5. The error in total thermal units due to errors  $dT_a$ ,  $d\epsilon_o$ , and  $dT$  was:

$$\begin{aligned} dI_i &= \partial I / \partial T_a dT_a + \partial I / \partial \epsilon_o d\epsilon_o + \partial I / \partial T dT \\ &= [\epsilon_o I_o + (\epsilon_o - 2) I_a] dT_a + [T_a I_o + (T_a - 1) I_a] d\epsilon_o \\ &\quad + [(I_i^2 B / AT^2) \exp(B/T)] \end{aligned} \quad (5-4)$$

Substituting in estimated values  $dT_a = 0.01$ ,  $d\epsilon_o = 0.01$ , and  $dT = 0.2$  °C and typical values for the  $I$  terms, the estimate of thermal value error was  $dI \sim 0.75$  t.u.

The subsequent error in temperature calculations due to thermal value error was:

$$dT = \partial T / \partial I_i dI_i = [(T^2 / I_i B) / (1 - I/A)] dI_i \quad (5-5)$$

Substituting typical values for temperature and thermal units, the estimated error in temperature measurements was  $dT \sim 1.0$  °C.

An additional error in temperature values was introduced during the process of making the 6 X 15 element temperature distributions from images displayed on the Thermovision's computer CRT. Depending on the range of the Point Sur, two to four CRT pixels were averaged to establish a temperature for each element in the 6 X 15 arrays. Temperatures varied by as much as 1 °C between CRT pixels. The estimated error attributed to this averaging process was 0.5 °C. Thus the total estimated temperature error was:

$$\begin{aligned}\text{Total error} &= \text{Measurement error} + \text{Averaging error} \\ &= 1.0 \text{ }^{\circ}\text{C} + 0.5 \text{ }^{\circ}\text{C} = 1.5 \text{ }^{\circ}\text{C}\end{aligned}$$

#### E. REVIEW OF REVISED THERMOVISION VS. THERMISTOR TEMPERATURE DIFFERENCES

The recalculated temperatures were also compared to the thermistor temperatures. These results are found in Table 9. Based on review of Table 9, Thermovision-computed temperatures agreed with thermistor temperatures (within experimental error) in 20 out of 26 cases during the four days of measurements. Six additional cases could not be compared because temperatures exceeded the Thermovision's thermal range setting.

In the six cases in which agreement did not exist, few conclusive trends about these anomalies could be established. These cases involved four different thermistors over the course of all four days. One notable observation was that in



five cases the Thermovision's predicted temperatures were much lower than the thermistor temperatures. Apparently the thermal radiation was partially shielded or severely attenuated in these cases.

A point that must be considered is that each thermistor was measuring an area of ship surface on the order of one square centimeter while each element in the Thermovision's temperature distributions corresponded to an area on the order of one square meter. Thus, any localized heat sources on the ship may have been obscured by more dominant ambient conditions.

#### F. MTF AND MRTD CURVES

One observation of the MTF/MRTD plots (Figures 4.10 and 4.11) was the cutoff frequency, i.e. the spatial frequency at which the Thermovision could no longer resolve a target. This frequency was 400 cycles/radian; however, this value has little utility because it corresponds to an infinite MRTD. A more practical frequency was the critical frequency which was determined by extending a line through the approximately straight portion of the MTF curve to the intercept of the frequency axis. This critical frequency was 360 cycles/radian which corresponded to an MRTD of 2.2 °C. As an illustrative example: the critical frequency would equate to a lateral distance of 1.4 m for a target at 1000 m. Thus, the Thermovision could resolve target structures to within

1.4 m provided that the target to background temperature was at least 2.2 °C.

The MRTD curve was also used to determine the MRTD of an element from the 6 X 15 element temperature distributions. Recalling that these elements represented 2.75 m width along the ship's length, the horizontal spatial frequency of an element is 182 cycles/radian at a target range of 1000 m. This frequency corresponds to an MRTD of 0.2 °C. An important observation is that this MRTD is much less than the uncertainty in temperature due to experimental error (1.5 °C). Thus, this pixel size did not limit the experiment. However, pixel size could be a factor if the MRTD was comparable to the temperature uncertainty. The limiting element size in this case would be 1.6 m based on an MRTD of 1.5 °C. Thus, the Point Sur with a length of 41.2 m could be divided into a maximum of 25 horizontal elements for temperature distributions.

A clarification at this point should be made with regard to vertical resolution. The system MRTD curve developed in this thesis was based on horizontal spatial frequencies; therefore, the analysis of vertical resolution was not possible in this thesis.

The Thermovision's computer displayed the system's 7° X 7° field of view with the array of 128 X 128 pixels. This pixel size corresponded to a spatial frequency of 525

cycles/radian. Thus, the image video would be limited by the Thermovision's components preceding the computer display.

A final observation of the MTF and MRTD plots was that these curves were very typical except for a portion of the MTF at the higher spatial frequencies. In this region the slope of the curve for a typical MTF would be monotonically decreasing. This was not the case for the Thermovision's MTF; however, this was most likely due to data scatter, rather than the Thermovision having atypical performance characteristics.

## VI. CONCLUSIONS AND RECOMMENDATIONS

### A. SUMMARY

Thermal images of the Point Sur were recorded at two locations on Monterey Bay with the AGA Thermovision 780. The Thermovision's temperature evaluation program was calibrated under laboratory conditions with a black body source set at known temperatures. This program was used to establish temperature distributions of the Point Sur images. These temperature distributions consisted of 6 X 15 element arrays which portrayed the ship's superstructure.

Temperatures from eight elements on these distributions were compared to temperatures measured by thermistors. These measurement devices had been installed during the recording of the ship's images and were located at eight points on the Point Sur that corresponded to the eight elements in the temperature distributions. A deduced correction was made to an equation used in the Thermovision's temperature evaluation program, so that Thermovision-computed temperatures agreed with thermistor-measured temperatures.

System CTF, MTF, and MRTD curves were also produced. The MRTD curve was used to determine the resolution limit of the Thermovision and to compare this limit with the resolution limit of the temperature distributions and the Thermovision's computer display.

## B. CONCLUSIONS

Initial comparison of target temperatures computed by the AGA Thermovision 780 and actual temperatures measured by thermistors revealed that the Thermovision underestimated actual temperatures on the four days on which data were recorded. Two modifications were made to an equation used by the Thermovision's computer to calculate target temperatures. The first modification was made based upon the assumption that the target's ambient atmosphere was essentially identical with the atmosphere between the target and Thermovision. This assumption had the implication that the ambient atmosphere's emissivity would be the same as the other portion of the atmosphere. The second modification was empirically determined and when used in conjunction with the first modification, good agreement existed between the Thermovision and thermistors to within 1.5 °C. In the few cases in which agreement clearly did not exist, the Thermovision underestimated target temperatures. This was attributed to the masking of target radiation rather than any measurement error introduced by the Thermovision.

The AGA Thermovision 780 MTF and MRTD curves produced from images of aluminum bar targets resembled the curves of a typical system depicted in Figure 2.8 except at the higher spatial frequencies of the MTF curve. The irregularities in this portion of the curve were attributed to data scatter associated with the very small target signals in these



frequencies. The Thermovision's cutoff frequency was determined to be 400 cycles/radian. The critical frequency was 360 cycles/radian at 2.2 °C MRTD.

Another important spatial frequency was that which corresponded to the width of an element in the temperature distributions. This frequency was 182 cycles/radian at 0.2 °C MRTD.

### C. RECOMMENDATIONS

While the Thermovision's temperature prediction capabilities proved satisfactory under various atmospheric conditions, further testing should be conducted to verify that changes to one of the system's temperature prediction equations are justified for other conditions.

The use of 6 X 15 arrays to depict the Point Sur's temperature distribution was viable but could be improved. First, the number of elements in these arrays could be increased in order to reduce the error introduced when several CRT pixels are averaged to determine a temperature for one array element. The maximum number of horizontal pixels would be limited to 25. The Thermovision's MRTD for this pixel size would equal the experimental error in temperature (1.5 °C). Second, an automated means of extracting temperature information from the Thermovision's computer is needed. The manual process of recording temperatures from the CRT screen and calculating average temperatures is tedious and time consuming.

The determination of the system MTF and MRTD curve could be improved by using an amplifier to increase the gain of the video entering the oscilloscope. This action would increase the accuracy of measuring radiation contrast and reduce data scatter at the higher spatial frequencies where target signals are quite small and difficult to measure. Also, the Thermovision should be evaluated using the MRTD test described in reference one and the results compared to a MRTD curve determined using the method presented in this thesis. Finally, MTF and MRTD curves should be developed for vertical spatial frequencies, so that the Thermovision's resolution characteristics in the vertical direction can be assessed.

Any further testing with the Thermovision should be done with the Thermal Level and Thermal Range settings adjusted so that the entire target distribution of a target can be determined. One limitation of this thesis has been the lack of temperature information around the Point Sur's smoke stack. This limitation was due to the Thermal Level being set too low, so that the highest temperatures on the ship's superstructure could not be measured.

## APPENDIX A

### FIGURES

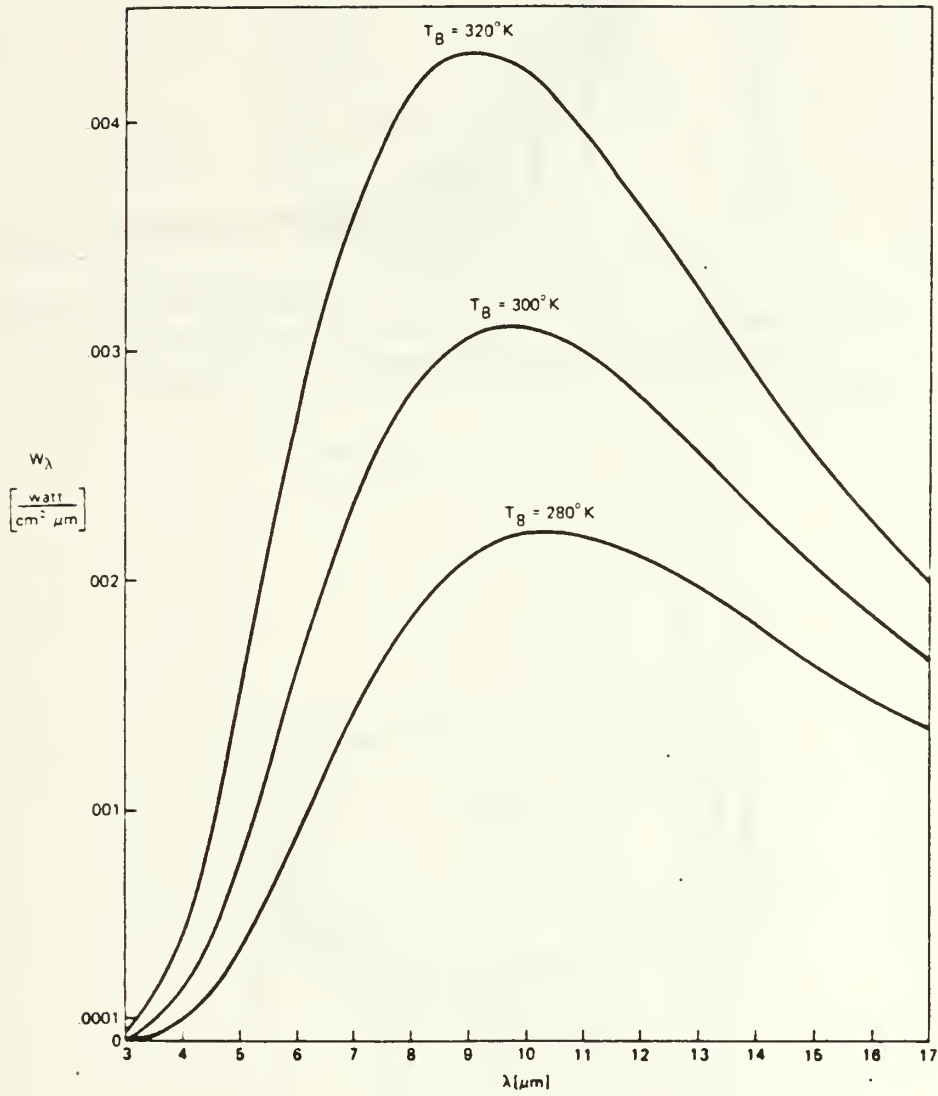


Figure 2.1 Planck's law for spectral radiant emittance

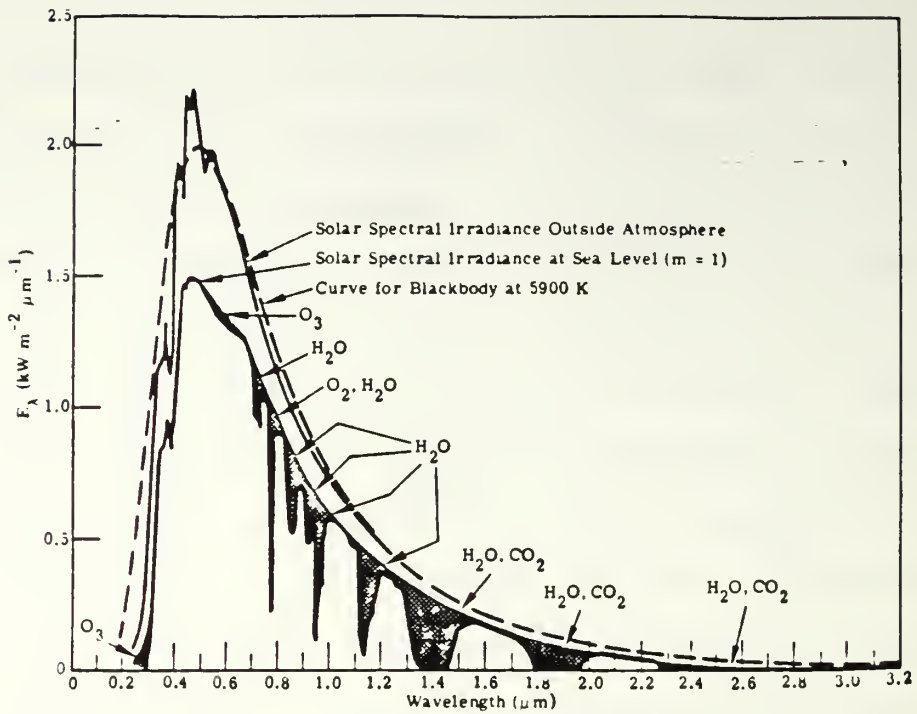


Figure 2.2 Spectral distribution curves related to the sun (Shaded areas indicate absorption due to atmospheric constituents)

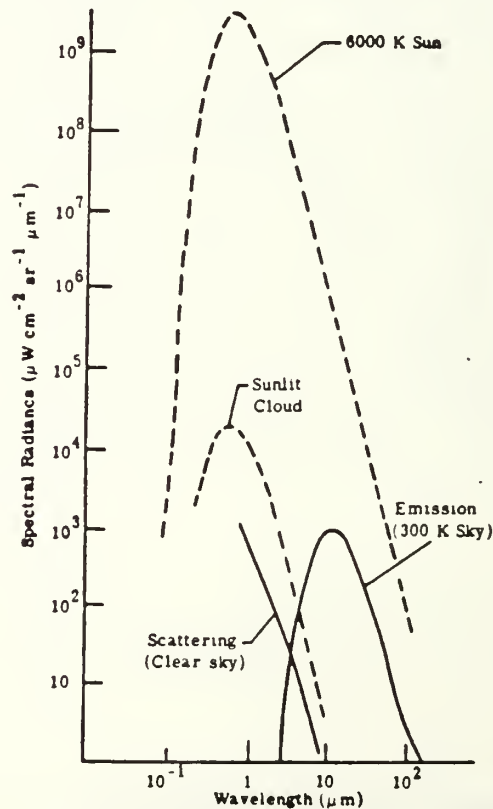


Figure 2.3 Contributions to background radiation in sky

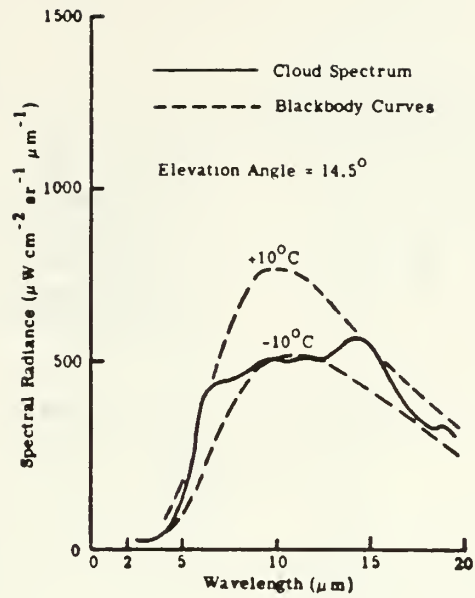


Figure 2.4 Spectral radiance of cumulus cloud

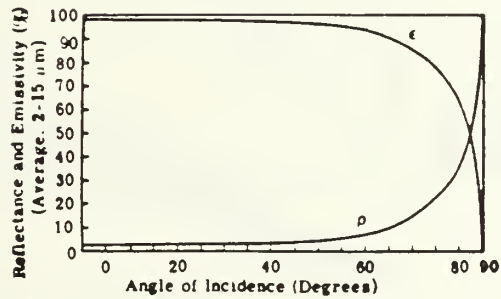


Figure 2.5 Reflectance and emissivity of water ( 2 to 15  $\mu\text{m}$  average) vs. angle of incidence



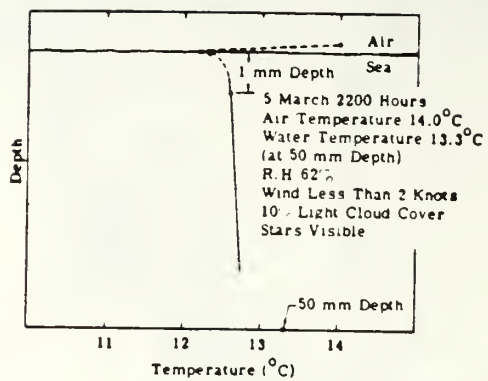


Figure 2.6 Thermal distribution of sea surface

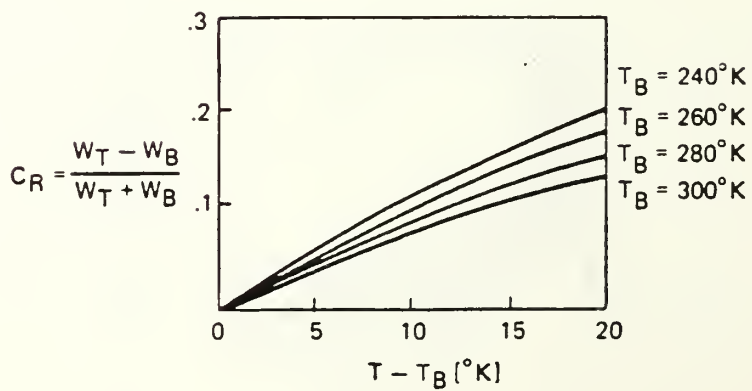


Figure 2.7 Radiation contrast for 8-14  $\mu m$  band

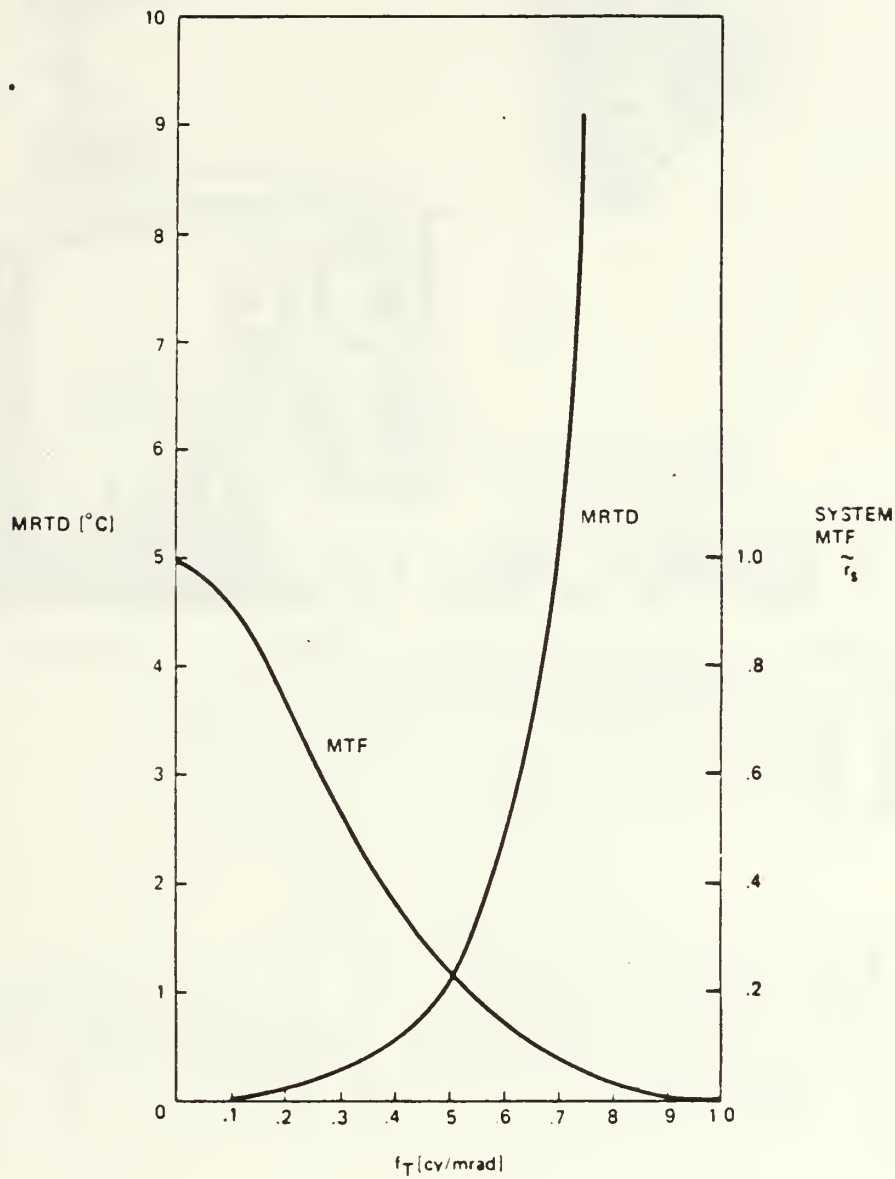


Figure 2.8 MTF and MRTD curves of thermal imaging system

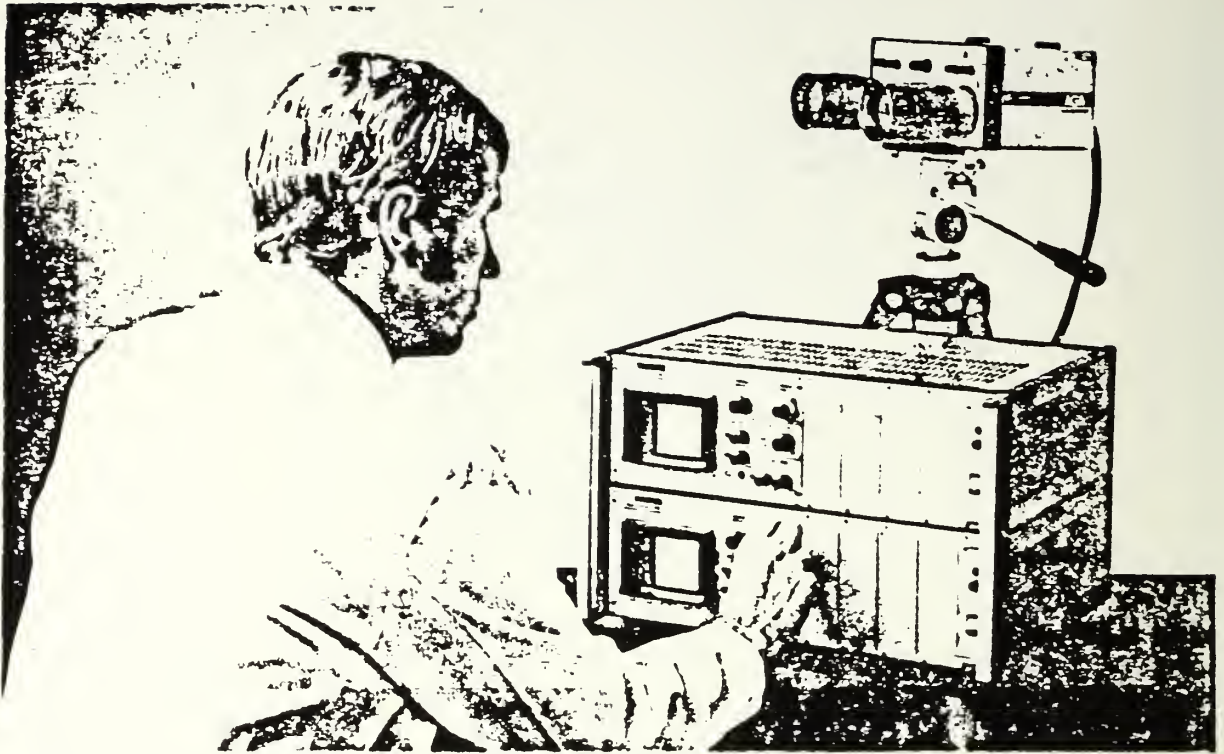


Figure 3.1 Thermovision dual scanner with black and white chassis monitor

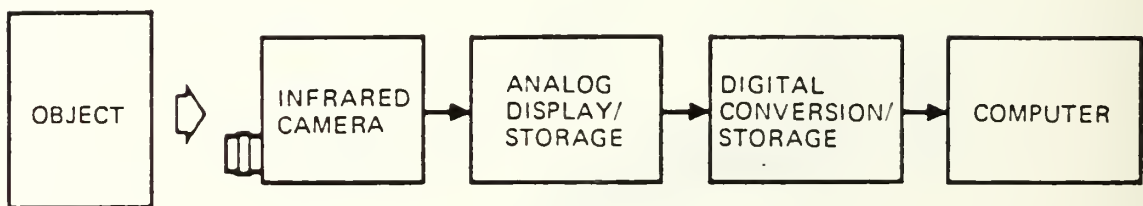


Figure 3.2 Schematic of total AGA Thermovision 780 system

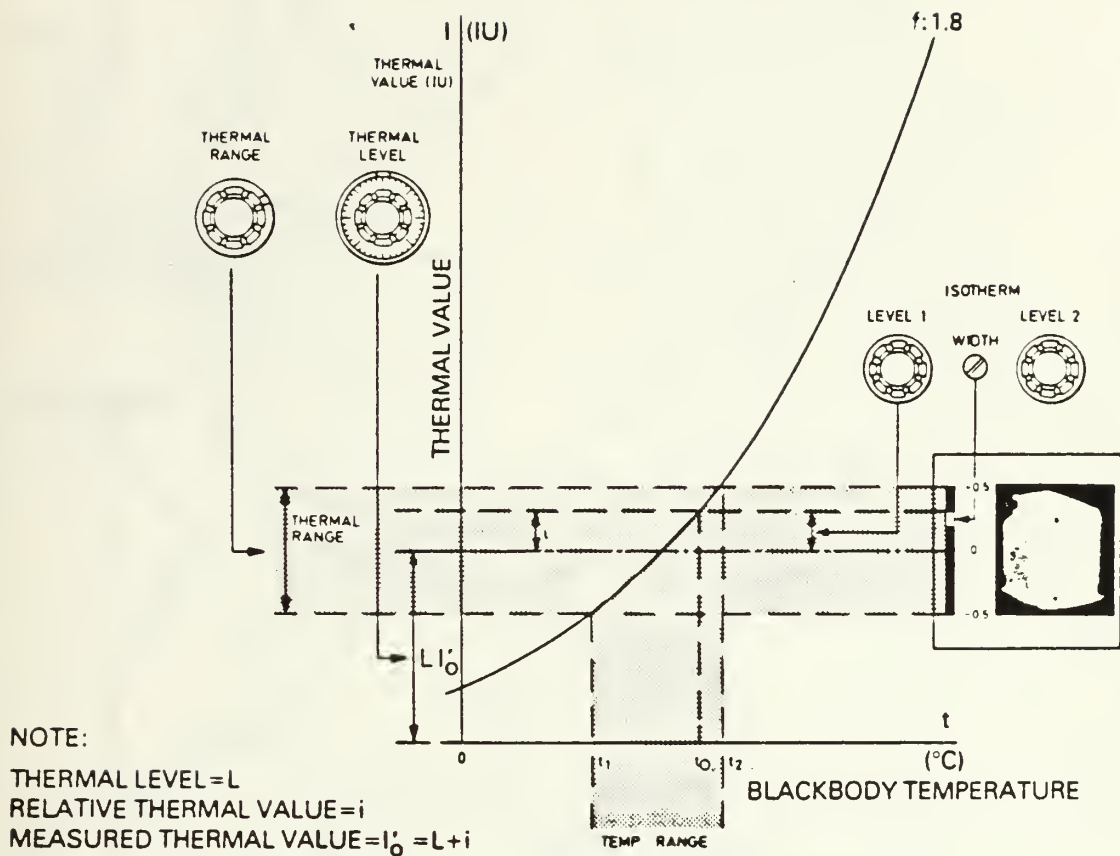
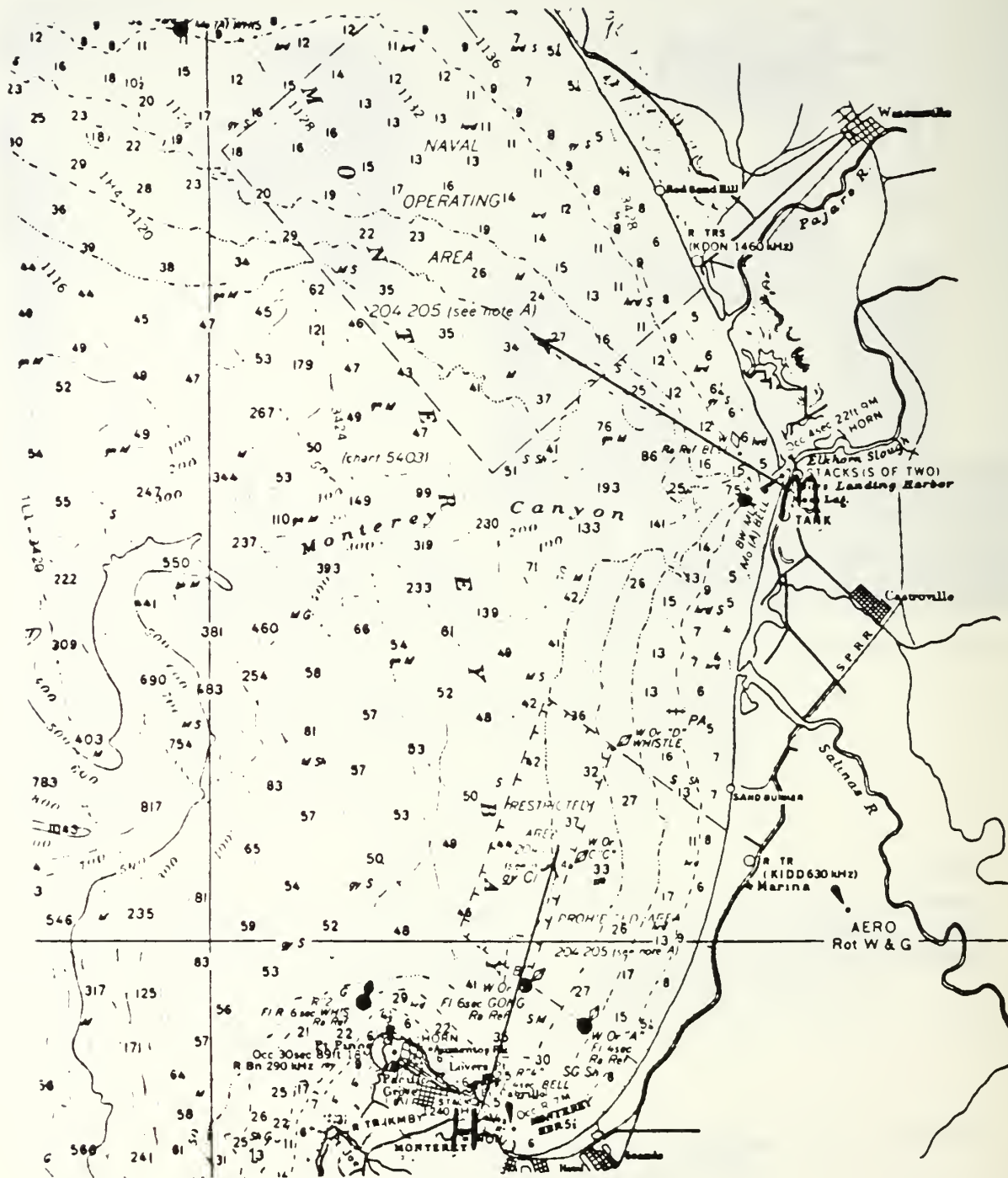


Figure 3.3 Thermal level and thermal range settings vs. black body temperature



M: Moss Landing Location  
H: Hopkins Marine Station Location

Figure 4.1 Locations of Thermovision and approximate direction of aim



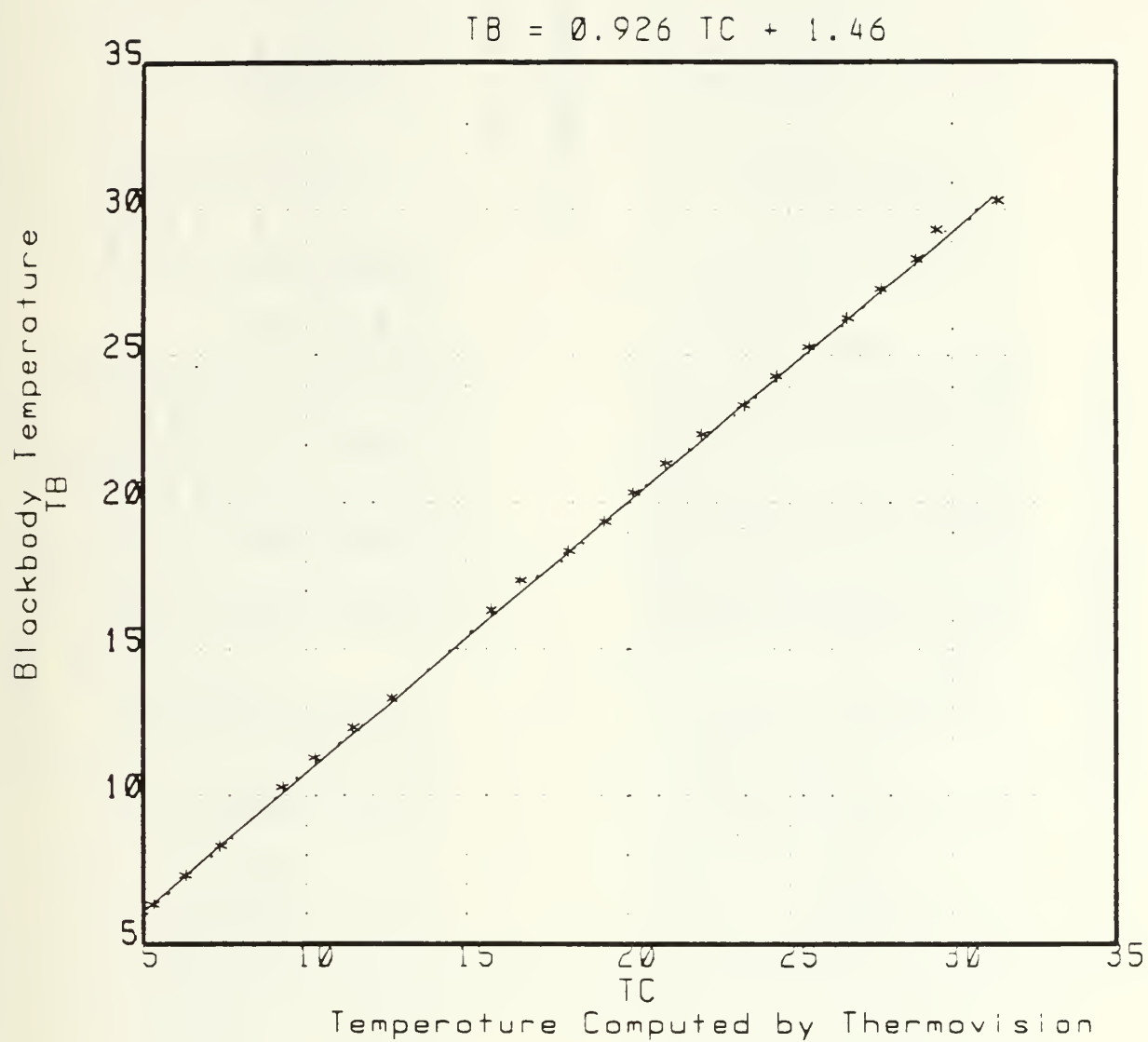


Figure 4.2 Thermovision supplemental calibration curve (°C)





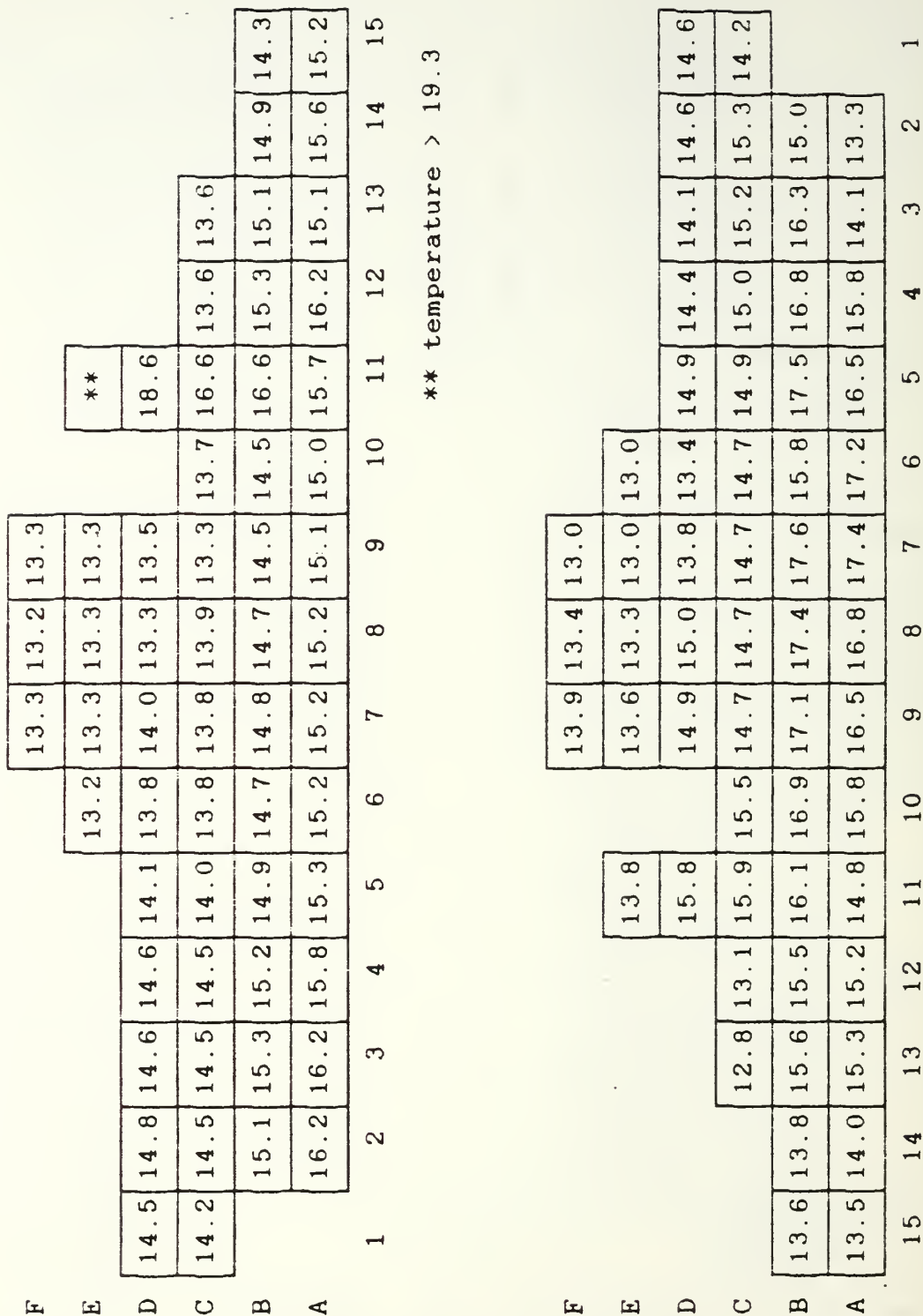
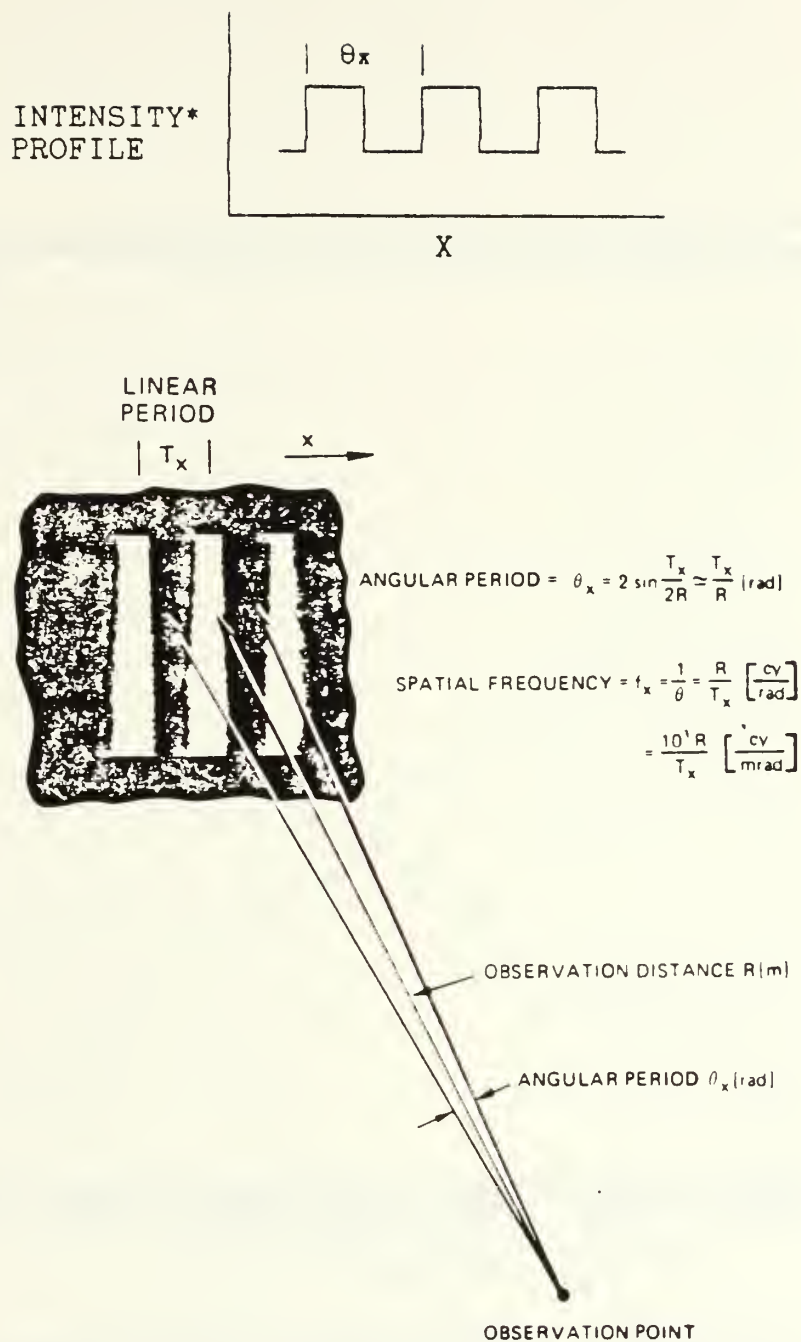


Figure 4.5 Point Sur temperature distribution (°C)  
11 May 1987









\* This portion of original figure has been modified.

Figure 4.8 Bar target pattern perceived by Thermovision

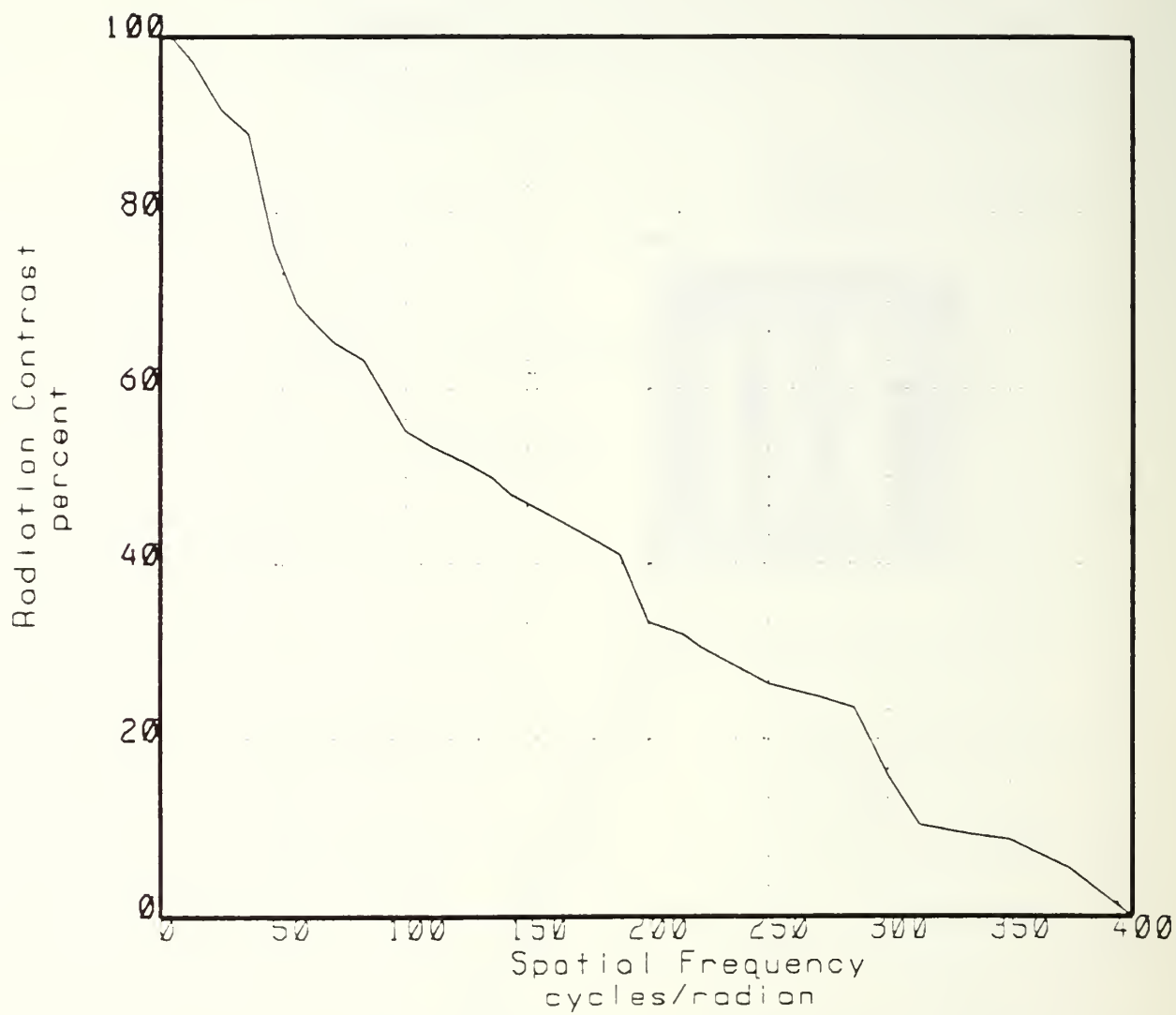


Figure 4.9 Thermovision system CTF curve

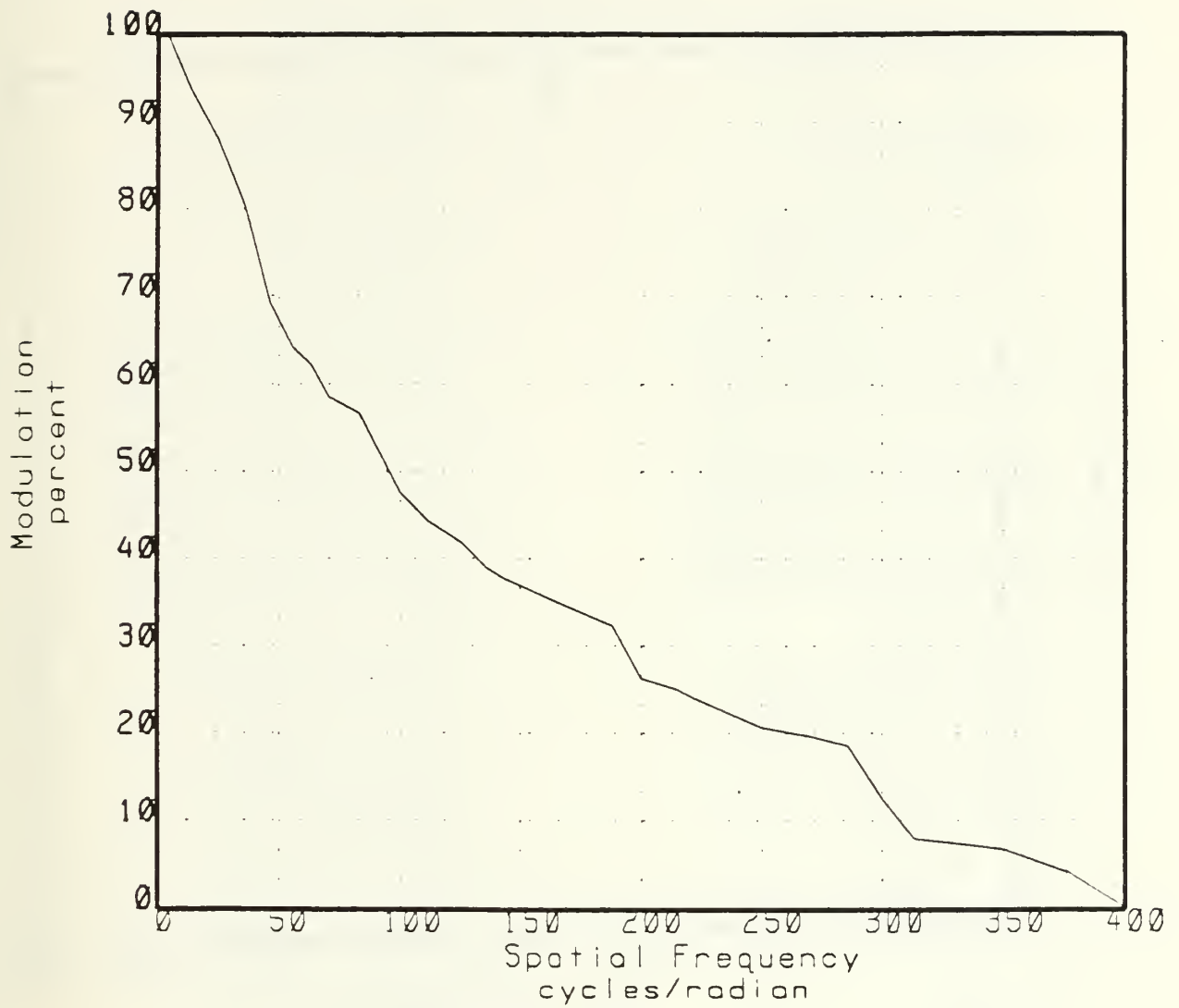


Figure 4.10 Thermovision system MTF curve

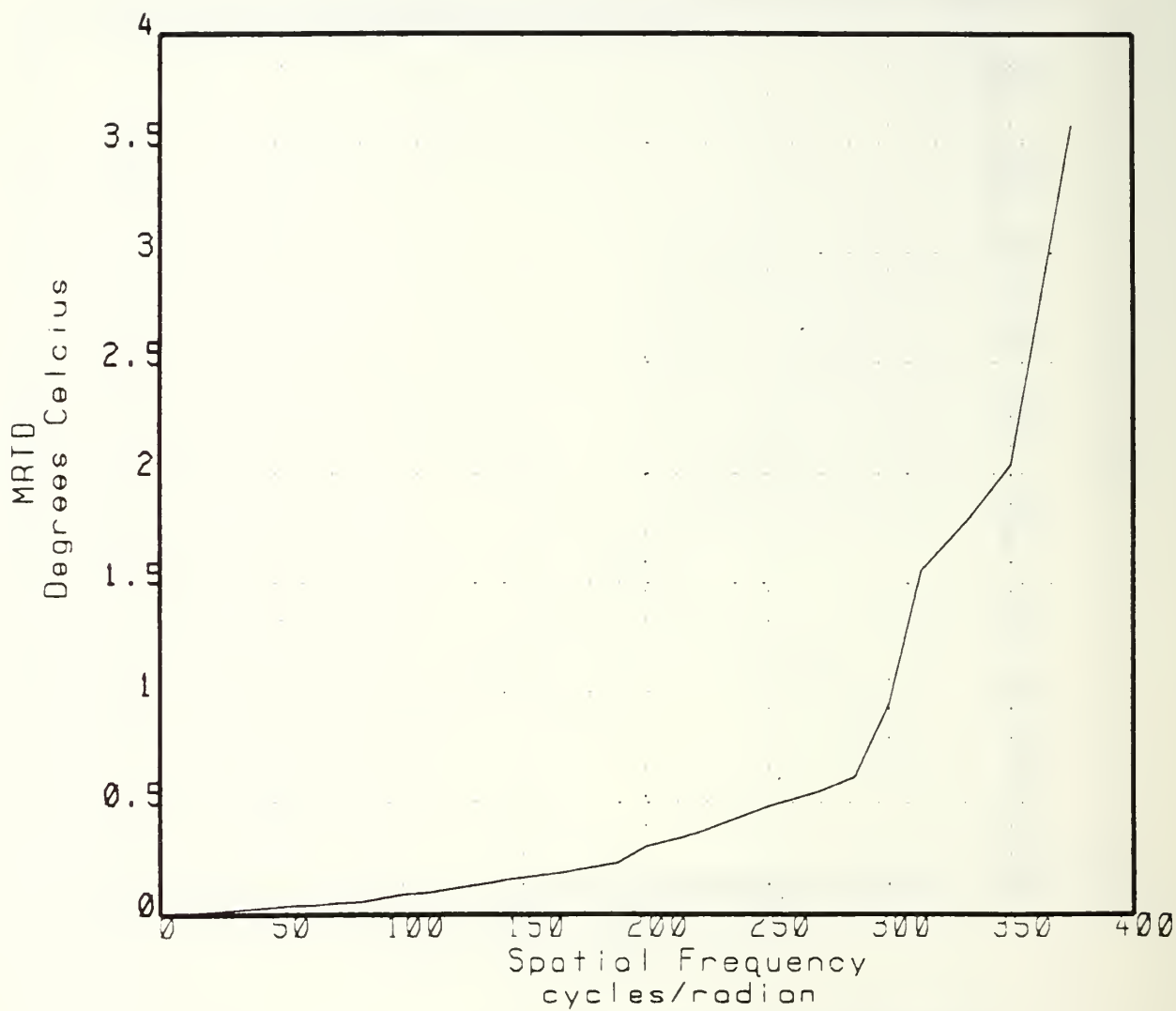


Figure 4.11 Thermovision system MRTD curve





[illegible]

**\*\* temperature > 21.8**

[illegible]

**\*\* temperature > 20.3**

Figure 5.2 Revised temperature distribution (°C)  
9 May 1987





# APPENDIX B

## TABLES

TABLE 1

### RADIOSONDE DATA

DATE	6 May	9 May	11 May	13 May
TIME OF LAUNCH	1905	0947	1009	1008
TEMPERATURE (°C)	15.31	11.61	12.31	14.01
DEW POINT (°C)	12.31	11.51	12.11	13.01
RELATIVE HUMIDITY (%)	82.20	99.61	99.01	93.91
PRESSURE (mbar)	1008.71	1015.31	1009.21	1006.51
WIND DIRECTION (degrees)	238.31	335.81	228.11	331.61
WIND SPEED (m/sec)	1.61	3.51	1.91	8.11
ALTITUDE (m)	29.01	10.01	34.01	55.01

TABLE 2

## TEMPERATURES AT SHIP AND TRANSMITTANCE VALUES

DATE	6 May	6 May	9 May	9 May
TIME	1855-1858	1859-1903	1126-1130	1138-1143
AIR TEMP. (°C)	14.5	14.5	12.0	12.0
SEA SURF. TEMP. (°C)	15.2	15.2	13.2	13.2
SHIP RANGE (m)	800	800	1000	1000
TRANSMITTANCE	0.91	0.89	0.67	0.62

DATE	11 May	11 May	13 May	13 May
TIME	0942-0950	1002-1010	1518-1523	1524-1528
AIR TEMP. (°C)	12.1	12.1	14.0	14.0
SEA SURF. TEMP. (°C)	13.4	13.4	15.0	15.0
SHIP RANGE (m)	800	800	700	700
TRANSMITTANCE	0.90	0.90	0.93	0.93

TABLE 3  
THERMOVISION SUPPLEMENTAL CALIBRATION DATA

BLACKBODY TEMPERATURE ( °C)	THERMOVISION MEASURED TEMPERATURE ( °C)	TEMPERATURE DIFFERENCE ( °C)
6.0 ± 0.1	5.1 ± 0.1	- 0.9 ± 0.1
7.0	6.1	- 0.9
8.0	7.2	- 0.8
9.0	15.8	+ 7.8*
10.0	9.1	- 0.9
11.0	10.1	- 0.9
12.0	11.3	- 0.7
13.0	12.5	- 0.5
14.0	12.5	- 1.5*
15.0	13.6	- 1.4*
16.0	15.6	- 0.4
17.0	16.5	- 0.5
18.0	18.0	0.0
19.0	19.1	+ 0.1
20.0	20.0	0.0
21.0	21.0	0.0
22.0	22.1	+ 0.1
23.0	23.4	+ 0.4
24.0	24.4	+ 0.4
25.0	25.4	+ 0.4
26.0	26.6	+ 0.6
27.0	27.6	+ 0.6
28.0	28.7	+ 0.7
29.0	29.3	+ 0.3
30.0	31.2	+ 1.2

\* Data point disregarded.



TABLE 4  
THERMISTOR DATA (°C)

DATE	6 May	6 May	9 May	9 May
TIME	1855-1858	1859-1903	1126-1130	1138-1143
THERMISTOR 1	16.48±0.10	16.31±0.13	16.55±0.30	15.58±0.16
THERMISTOR 2	17.39±0.13	16.97±0.18	17.71±0.17	17.00±0.17
THERMISTOR 3	21.11±0.22	20.94±0.12	17.41±0.11	17.67±0.14
THERMISTOR 4	17.33±0.10	17.17±0.10	17.25±0.23	16.72±0.15
THERMISTOR 5	18.71±0.27	18.64±0.29	18.22±0.27	18.67±0.22
THERMISTOR 6	17.29±0.12	16.94±0.15	17.81±0.18	17.22±0.13
THERMISTOR 7	24.05±0.34	24.29±0.55	34.63±0.24	33.58±0.38
THERMISTOR 8	21.76±0.13	21.76±0.20	33.22±0.80	28.16±0.40
DATE	11 May	11 May	13 May	13 May
TIME	0942-0950	1002-1010	1518-1523	1524-1528
THERMISTOR 1	15.41±0.15	15.23±0.12	18.39±0.16	17.96±0.19
THERMISTOR 2	15.96±0.08	15.89±0.12	19.31±0.27	18.33±0.19
THERMISTOR 3	16.07±0.06	15.92±0.06	18.85±0.15	20.23±0.29
THERMISTOR 4	15.79±0.11	15.68±0.11	20.58±0.20	20.10±0.12
THERMISTOR 5	15.23±0.19	14.95±0.22	26.97±0.07	27.42±0.15
THERMISTOR 6	16.89±0.13	16.90±0.10	20.15±0.41	18.61±0.16
THERMISTOR 7	35.62±0.23	34.57±0.31	39.50±0.18	41.36±0.59
THERMISTOR 8	39.15±0.52	38.24±0.19	39.66±0.78	37.34±0.51

TABLE 5  
TEMPERATURE DIFFERENCE (°C)  
(THERMOVISION TEMPERATURES-THERMISTOR TEMPERATURES)

DATE	6 May	9 May	11 May	13 May
THERMISTOR 1	- 3.4	- 1.3	+ 1.8	- 3.3
THERMISTOR 2	- 3.4	- 1.3	- 1.4	- 3.2
THERMISTOR 3	- 6.2	- 3.9	- 1.2	- 3.2
THERMISTOR 4	- 3.1	- 1.8	- 1.4	- 3.9
THERMISTOR 5	- 5.3	- 2.0	- 1.4	-12.1
THERMISTOR 6	- 3.2	- 1.0	- 2.7	- 2.7
THERMISTOR 7	- 8.2	*	*	*
THERMISTOR 8	- 3.2	*	*	*

\* Not available.

TABLE 6  
RADIATION CONTRAST  
(Target Temperature = 25.0 °C, Room Temperature = 18.8 °C)

SPATIAL FREQUENCY* (cycles/radian)	H <sub>max</sub> (cm)	H <sub>min</sub> (cm)	C** (%)
4.00 ± 0.05	1.40 ± 0.02	0.20 ± 0.02	75.0 ± 1.9
13.0 ± 0.2	1.40	0.22	72.8 ± 2.0
25.0 ± 0.5	1.40	0.26	68.7 ± 2.2
36.0 ± 0.9	1.40	0.28	66.7 ± 2.5
46.0 ± 1.3	1.40	0.38	57.3 ± 2.3
56.0 ± 1.8	1.40	0.44	52.2 ± 2.2
63.0 ± 2.2	1.40	0.46	50.5 ± 2.3
71.0 ± 2.8	1.40	0.48	48.9 ± 2.4
83.0 ± 3.6	1.40	0.50	47.4 ± 2.6
100 ± 5	1.40	0.58	41.4 ± 2.5
111 ± 3	1.40	0.60	40.0 ± 1.5
125 ± 4	1.40	0.62	38.6 ± 1.6
136 ± 3	1.40	0.64	37.3 ± 1.2
143 ± 5	1.40	0.66	35.9 ± 1.6
167 ± 6	1.40	0.70	33.3 ± 1.5
188 ± 5	1.40	0.74	30.8 ± 1.1
200 ± 9	1.40	0.84	25.0 ± 1.3
215 ± 7	1.40	0.86	23.9 ± 1.0
222 ± 5	1.40	0.88	22.8 ± 0.7
250 ± 9	1.40	0.94	19.7 ± 0.9
271 ± 10	1.40	0.96	18.6 ± 0.8
286 ± 9	1.40	0.98	17.6 ± 0.7
300 ± 13	1.40	1.10	12.0 ± 0.6
313 ± 11	1.40	1.20	7.69 ± 0.33
333 ± 12	1.36	1.18	7.09 ± 0.31
350 ± 15	1.30	1.14	6.56 ± 0.33
375 ± 16	0.65	0.60	4.00 ± 0.23
400 ± 17	0.60	0.60	0.00

\*  $df = (1/2w)dR + (R/2w^2)dw$

Where df is estimated frequency error, w is bar width, R is range target, dw = 0.0002 m, and dR = 0.01 m.

\*\*  $dC = [2(H_{max}-H_{min})/(H_{max}+H_{min})^2] dH + (df/f)C$

Where dC is estimated radiation contrast error.

TABLE 7  
NORMALIZED RADIATION CONTRAST AND MTF

SPATIAL FREQUENCY (cycles/radian)	NORMALIZED C (%)	MTF* (%)
4.00 ± 0.05	100 ± 3	99.7 ± 3.0
13.0 ± 0.2	97.1 ± 2.7	93.9 ± 2.7
25.0 ± 0.5	91.6 ± 2.9	88.0 ± 2.9
36.0 ± 0.9	88.9 ± 3.3	80.3 ± 3.3
46.0 ± 1.3	76.4 ± 3.1	69.2 ± 3.1
56.0 ± 1.8	69.6 ± 2.9	64.0 ± 2.9
63.0 ± 2.2	67.4 ± 3.1	62.1 ± 3.1
71.0 ± 2.8	65.2 ± 3.2	58.4 ± 3.2
83.0 ± 3.6	63.2 ± 3.5	56.5 ± 3.5
100 ± 5	55.2 ± 3.3	47.5 ± 3.3
111 ± 3	53.3 ± 2.0	44.3 ± 2.0
125 ± 4	51.5 ± 2.1	41.8 ± 2.1
136 ± 3	49.7 ± 1.6	39.0 ± 1.6
143 ± 5	47.9 ± 2.1	37.6 ± 2.1
167 ± 6	44.4 ± 2.0	34.9 ± 2.0
188 ± 5	41.1 ± 1.5	32.3 ± 1.5
200 ± 9	33.3 ± 1.7	26.2 ± 1.7
215 ± 7	31.9 ± 1.3	25.1 ± 1.3
222 ± 5	30.4 ± 0.9	23.9 ± 0.9
250 ± 9	26.2 ± 1.2	20.6 ± 1.2
271 ± 10	24.9 ± 1.1	19.6 ± 1.1
286 ± 9	23.5 ± 0.9	18.5 ± 0.9
300 ± 13	16.0 ± 0.8	12.6 ± 0.8
313 ± 11	10.3 ± 0.4	8.09 ± 0.40
333 ± 12	9.45 ± 0.40	7.42 ± 0.40
350 ± 15	8.75 ± 0.40	6.87 ± 0.40
375 ± 16	5.33 ± 0.30	4.19 ± 0.30
400 ± 17	0.00	

\*  $dMTF = dC$   
Where  $dMTF$  is the estimated MTF error.

TABLE 8  
MTF AND MRTD

SPATIAL FREQUENCY (cycles/radian)	MTF (%)	MRTD* (°C)
4.00 ± 0.05	99.7 ± 3.0	1.60 ± 0.07 X 10 <sup>-3</sup>
13.0 ± 0.2	93.9 ± 2.7	5.55 ± 0.24 X 10 <sup>-3</sup>
25.0 ± 0.5	88.0 ± 2.9	1.14 ± 0.06 X 10 <sup>-2</sup>
36.0 ± 0.9	80.3 ± 3.3	1.79 ± 0.12 X 10 <sup>-2</sup>
46.0 ± 1.3	69.2 ± 3.1	2.66 ± 0.19 X 10 <sup>-2</sup>
56.0 ± 1.8	64.0 ± 2.9	3.50 ± 0.27 X 10 <sup>-2</sup>
63.0 ± 2.2	62.1 ± 3.1	4.08 ± 0.30 X 10 <sup>-2</sup>
71.0 ± 2.8	58.4 ± 3.2	4.86 ± 0.46 X 10 <sup>-2</sup>
83.0 ± 3.6	56.5 ± 3.5	5.88 ± 0.61 X 10 <sup>-2</sup>
100 ± 5	47.5 ± 3.3	8.42 ± 1.01 X 10 <sup>-2</sup>
111 ± 3	44.3 ± 2.0	1.00 ± 0.07 X 10 <sup>-1</sup>
125 ± 4	41.8 ± 2.1	1.20 ± 0.10 X 10 <sup>-1</sup>
136 ± 3	39.0 ± 1.6	1.39 ± 0.09 X 10 <sup>-1</sup>
143 ± 5	37.6 ± 2.1	1.52 ± 0.14 X 10 <sup>-1</sup>
167 ± 6	34.9 ± 2.0	1.91 ± 0.18 X 10 <sup>-1</sup>
188 ± 5	32.3 ± 1.5	2.33 ± 0.17 X 10 <sup>-1</sup>
200 ± 9	26.2 ± 1.7	3.05 ± 0.34 X 10 <sup>-1</sup>
215 ± 7	25.1 ± 1.3	3.43 ± 0.29 X 10 <sup>-1</sup>
222 ± 5	23.9 ± 0.9	3.72 ± 0.22 X 10 <sup>-1</sup>
250 ± 9	20.6 ± 1.2	4.85 ± 0.46 X 10 <sup>-1</sup>
271 ± 10	19.6 ± 1.1	5.53 ± 0.51 X 10 <sup>-1</sup>
286 ± 9	18.5 ± 0.9	6.18 ± 0.50 X 10 <sup>-1</sup>
300 ± 13	12.6 ± 0.8	9.52 ± 1.02 X 10 <sup>-1</sup>
313 ± 11	8.09 ± 0.40	1.56 ± 0.13
333 ± 12	7.42 ± 0.40	1.80 ± 0.16
350 ± 15	6.87 ± 0.40	2.04 ± 0.21
375 ± 16	4.19 ± 0.30	3.58 ± 0.31
400 ± 17	0.00	

\*  $dMRTD = (4.00 \times 10^{-4}) [df/MTF + (f/MTF^2) dMTF]$   
Where dMRTD is the estimated MRTD error.

TABLE 9  
 REVISED TEMPERATURE DIFFERENCE (°C)  
 (THERMOVISION TEMPERATURES - THERMISTOR TEMPERATURES)

DATE	6 May	9 May	11 May	13 May
THERMISTOR 1	- 0.4	- 0.3	+ 2.0	- 0.9
THERMISTOR 2	- 1.0	- 0.1	+ 0.9	- 0.8
THERMISTOR 3	- 3.9	- 2.9	+ 0.9	- 0.8
THERMISTOR 4	- 0.7	- 0.4	+ 0.7	- 1.4
THERMISTOR 5	- 2.9	- 0.8	+ 0.9	- 9.7
THERMISTOR 6	- 0.8	- 0.2	- 0.3	- 0.3
THERMISTOR 7	- 6.3	*	*	*
THERMISTOR 8	- 0.9	*	*	*

\* Not available.



## LIST OF REFERENCES

1. Lloyd, J.M., Thermal Imaging Systems, Plenum Press, 1975.
2. Wolfe, William L. and Zissis, George J., The Infrared Handbook, Office of Naval Research, Department of Navy, 1978.
3. Cooper, A.W., PH 4253 classroom notes, Naval Postgraduate School, Monterey, California, 1987.
4. RCA Electro-Optics Handbook, Technical Series EOH-11, RCA Corporation, May 1978.
5. Due, Christopher T., Optical-Mechanical Active/Passive Imaging Systems - Volume II, p. 18, Office of Naval Research, Department of Navy, May 1982.
6. AGA Thermovision 780 information catalogue, publication number 556 556 538, AGA Infrared Systems AB, 1979.
7. Warren, C. and Frojdh, A., AGA Infrared Systems Computer Interfacing Guidebook, p. 9, AGA Corporation, 1977.
8. AGA Thermovision 780 Operating Manual, publication number 556 556 492, AGA Infrared Systems AB, 1980.
9. Dimitriadis, George, Thermal Image Measurements of Infrared Signatures, p. 69, Masters Thesis, Naval Postgraduate School, Monterey, California, December 1986.
10. Weast, Robert C., CRC Handbook of Chemistry and Physics, p. E-230, CRC Press, Inc., 1977.

# INITIAL DISTRIBUTION LIST

	No. Copies
1. Defense Technical Information Center Cameron Station Alexandria, Virginia 22304-6145	2
2. Library Code 0142 Naval Postgraduate School Monterey, California 93943-5002	2
3. Department Chairman, Code 61 Department of Physics Naval Postgraduate School Monterey, California 93943	1
4. Prof. A.W. Cooper 61Cr Department of Physics Naval Postgraduate School Monterey, California 93943	2
5. Prof. E.C. Crittenden, Code 61Ct Department of Physics Naval Postgraduate School Monterey, California 93943	1
6. Department of Navy Naval Environmental Prediction Research Facility Weapons Effects Assessment Division ATTN: John Cook Monterey, California 93943-5006	1
7. CPT Tim R. McKaig 429 Gardner Court Marion, Indiana 46942	1













Thesis  
M189  
c.1

Thesis  
M18963  
c.1

McKaig  
Thermal imaging  
with AGA Thermovision  
780.

4 JUN 92

37224

Thesis

M18963  
c.1

McKaig  
Thermal imaging with  
AGA Thermovision 780.



thesM18963

Thermal imaging with AGA Thermovision 78



3 2768 000 77494 701  
DUDLEY KNOX LIBRARY